

Exploring IMF Sampling Effects on Star Formation and Metallicity in Ultra-Faint Dwarf Galaxies

Myoungwon Jeon^{1,2*} and Minsung Ko¹

¹*School of Space Research, Kyung Hee University, 1732 Deogyong-daero, Yongin-si, Gyeonggi-do 17104, Korea*

²*Department of Astronomy & Space Science, Kyung Hee University, 1732 Deogyong-daero, Yongin-si, Gyeonggi-do 17104, Korea*

Accepted XXX. Received YYY; in original form ZZZ

ABSTRACT

We examine the impact of various Initial Mass Function (IMF) sampling methods on the star formation and metal enrichment histories of Ultra-Faint Dwarf (UFD) galaxy analogs. These analogs are characterized by $M_{\text{vir}} \approx 10^8 M_{\odot}$ and $M_* \lesssim 10^5 M_{\odot}$ at $z = 0$, utilizing high-resolution cosmological hydrodynamic zoom-in simulations with a gas particle mass resolution of $\sim 63 M_{\odot}$. Specifically, we evaluate three IMF sampling techniques: the burst model, stochastic IMF sampling, and individual IMF sampling. Our results demonstrate that the choice of IMF sampling method critically affects stellar feedback dynamics, particularly supernova (SN) feedback, thus impacting the star formation and metallicity characteristics of UFD analogs. We find that simulations with stochastic IMF sampling yield UFD analogs with 40% to 70% higher stellar masses than those using the burst model, due to a less immediate suppression of star formation by SNe. The individual IMF method results in even greater stellar masses—8% to 58% more than stochastic runs—as stars form individually and continuously. Star formation is most continuous with individual sampling, followed by stochastic, and least with the burst model, which shows the longest quenching periods. Furthermore, the individual sampling approach achieves higher metallicity stars, aligning well with observed values, unlike the lower metallicities—about 1 dex less—found in the burst and stochastic methods. This difference is attributed to the continuous star formation in individual sampling, where gas metallicity shaped by previous SN events is immediately reflected in stellar metallicity. These findings emphasize the essential role of choosing appropriate IMF sampling methods for accurately modeling the star formation and chemical evolution of UFD galaxies.

Key words: galaxies: formation – galaxies: dwarf – galaxies: star formation – methods: numerical

1 INTRODUCTION

Dwarf galaxies ($M_{\text{vir}} \lesssim 10^9 M_{\odot}$) are considered excellent laboratories for studying galaxy formation, as they are essential components in the hierarchically evolving Lambda cold dark matter (Λ CDM) Universe (reviewed in [Simon 2019](#); see also [Tolstoy et al. 2009](#); [McConnachie 2012](#)). Unlike massive systems such as the Milky Way (MW) galaxy, low-mass dwarfs are vulnerable to baryonic feedback due to their shallow gravitational potential wells, which allow gas to escape easily into the intergalactic medium (IGM). The simplicity of ultra-faint dwarfs (UFDs)—the smallest ($M_* \lesssim 10^5 M_{\odot}$) and most metal-poor ($[\text{Fe}/\text{H}] < -2$) galaxies in the Universe—provides valuable insights into how stellar feedback regulates the star formation histories (SFHs) of low-mass galaxies (e.g., [Sales et al. 2022](#); [Collins & Read 2022](#)).

UFDs tend to exhibit bursty star formation activity, followed by early quenching during or even before cosmic reionization, leading to relatively brief SFHs (e.g., [Bullock et al. 2000](#); [Bovill & Ricotti 2009](#); [Brown et al. 2014](#); [Weisz et al. 2014](#); [Gallart et al. 2021](#); [Savino et al. 2023](#); [Azartash-Namin et al. 2024](#)). Specifically, photoionization heating by stars and outflows caused by supernova (SN) explosions are primarily responsible for this bursty star formation

(e.g., [Simpson et al. 2013](#); [Jeon et al. 2017](#); [Zhang et al. 2024](#)). Consequently, UFDs are likely to cease star formation as the gas within their haloes evaporates, with little chance of re-infall due to global heating during reionization. Moreover, the host environment—such as tidal interactions or ram pressure stripping as UFDs fall into their host halo—also plays a crucial role in suppressing star formation (e.g., [Simpson et al. 2018](#); [Carlin et al. 2019](#); [Akins et al. 2021](#)). Thus, UFDs are more sensitive to baryonic feedback, necessitating sophisticated sub-grid models to describe star formation and the accompanying stellar feedback, which are essential for accurately simulating UFD analogs.

Numerous theoretical studies have explored the formation and evolution of UFD analogs, both as satellite galaxies of the MW or M31 (e.g., [Sawala et al. 2010](#); [Wetzel et al. 2015](#); [Applebaum et al. 2021](#)) and as isolated systems (e.g., [Simpson et al. 2013](#); [Oñorbe et al. 2015](#); [Wheeler et al. 2015, 2019](#); [Jeon et al. 2017](#); [Rey et al. 2019, 2020](#); [Agertz et al. 2020](#); [Sanati et al. 2023](#); [Goater et al. 2024](#)), using hydrodynamic simulations. In the context of assembling a MW-mass galaxy ($M_{\text{vir}} \approx 10^{12} M_{\odot}$), the mass of individual dark matter (DM) or baryon particles has been too large to resolve low-mass systems, including UFDs. Due to this limitation, high-resolution simulations have often been conducted for isolated UFDs, with recent advances in numerical techniques allowing for gas mass resolutions as low as a few tens of M_{\odot} (e.g., [Wheeler et al. 2019](#); [Agertz et al. 2020](#); [Rey](#)

* E-mail: myjeon@khu.ac.kr

et al. 2020; Jeon et al. 2021a). As numerical resolution improves, it becomes crucial to assess whether the sub-grid recipes previously adopted remain valid (e.g., Revaz et al. 2016; Hu et al. 2017; Su et al. 2018; Emerick et al. 2019; Applebaum et al. 2020; Andersson et al. 2023; Brauer et al. 2024).

In most galaxy simulations to date, star particles are typically represented as single stellar populations (SSPs), with stars distributed according to a specified initial mass function (IMF) (e.g., Katz 1992; Navarro & White 1993). This method averages the effects of stellar feedback across the IMF, influencing the interstellar medium (ISM) and the subsequent evolution of the galaxy. While this approach is effective for low-resolution simulations of larger galaxies, it may not be suitable for high-resolution simulations aimed at resolving UFDs, where gas particle masses range from a few tens to a thousand solar masses ($10 - 1000 M_{\odot}$). As noted by Revaz et al. (2016), stars cannot fully populate an IMF when the gas particle mass is below $1000 M_{\odot}$ (also see e.g., Hu et al. 2017). This creates a significant challenge when stars form from low-mass gas particles: the number of SNe occurring within a single numerical timestep might be less than one. As a result, the energy from a single SN event is distributed over multiple timesteps, significantly reducing the effectiveness of SN feedback compared to scenarios where SN energy is released explosively in a single timestep (e.g., Stinson et al. 2007; Durier & Dalla Vecchia 2012).

Beyond the conventional IMF-averaged approach, several alternative methods have been developed to manage SN energy release during the formation of low-mass galaxies. One such method is the burst model, which addresses the previously mentioned issue by releasing all the SN energy from a SSP simultaneously into the surrounding environment while still continuously distributing stars according to a given IMF. This ensures a substantial impact of SN explosions on the ISM, although it might be excessively intense, potentially impeding further star formation. Another approach is the stochastic IMF sampling method, where star masses are selected randomly rather than being fully distributed according to an IMF (e.g., Stinson et al. 2010; Hopkins et al. 2014; Revaz et al. 2016; Smith et al. 2018). This results in a varying number of high-mass stars that end as SNe for each star particle, influencing the intensity of SN feedback and shaping the SFHs of UFD analogs. This method is particularly suitable for simulating UFD analogs because it mirrors the discrete nature of SN events, allowing for individual explosions with a time delay during a single starburst, thus releasing SN energy in a discrete manner.

Recently, with enhanced resolution and star particle masses under ($m_{*} < 100 M_{\odot}$), a novel IMF sampling method has been proposed, involving the individual extraction of stars from specified IMFs. In this approach, each massive star capable of becoming an SN is represented by a single star particle (e.g., Emerick et al. 2019; Gutcke et al. 2021; Andersson et al. 2023; Deng et al. 2024; Brauer et al. 2024). Unlike the SSP method, this allows individually formed star particles to better reflect the specific conditions of the gas, such as the immediate aftermath of previous SNe and the metallicity of the gas.

In our previous papers (Jeon et al. 2017, 2021a,b), we studied the formation of dwarf galaxies ($M_{\text{vir}} \approx 10^8 - 10^9 M_{\odot}$) by conducting cosmological hydrodynamic zoom-in simulations, tracking their evolution from the time of the first stars, known as Population III (Pop III) stars, to the present day ($z = 0$). These simulations incorporated crucial baryonic processes, including SN feedback and the effects of reionization. For IMF sampling, we used the burst model, which releases the total SN energy into the ISM in a single event. This significantly impacted the surrounding environment and potentially overly suppressed subsequent star formation. Despite this, we found that the

physical characteristics of the simulated dwarfs (i.e., $M_{\text{vir}} - M_{*}$ and $M_{*} - [\text{Fe}/\text{H}]$ relationships) closely matched those observed in dwarf spheroidals (dSphs) within the MW galaxy. However, as previously mentioned, the physical properties of the simulated dwarfs can vary depending on the IMF sampling method employed.

While IMF sampling plays a critical role in high-resolution simulations, there has been limited research comparing various IMF sampling methods in the context of dwarf galaxy formation (e.g., Revaz et al. 2016; Hu et al. 2017; Su et al. 2018; Applebaum et al. 2020). For instance, Applebaum et al. (2020) explored two IMF sampling strategies—stochastic IMF sampling and the IMF-averaged method—by implementing them in cosmological hydrodynamic simulations of MW-like galaxies and isolated dwarf galaxies at $z = 6$. They suggested that the discrete SN feedback from stochastic IMF sampling tends to result in more bursty star formation compared to the continuous SN feedback from a fully populated IMF. This can cause an earlier suppression of star formation, especially in smaller dwarf galaxies ($M_{\text{vir}} \lesssim 10^{8.5} M_{\odot}$), leading to lower stellar masses in dwarf galaxies with the stochastic IMF compared to those employing the continuous IMF. In addition, Smith (2021) investigated the impact of SN feedback, photoionization heating by stars, and photoelectric heating of dust grains by assuming two different models: stochastic IMF and IMF-averaged rate. They simulated idealized isolated dwarf galaxies with $M_{\text{vir}} \sim 10^{10} M_{\odot}$ and emphasized that the choice of IMF sampling method has significant effects on the results, particularly when considering photoionization heating by stars.

Stellar metallicity is another crucial property of simulated UFD analogs, which is influenced by the method of star sampling and the way SN energy is distributed into the ISM. High-resolution simulations of UFD analogs show that it is challenging to evolve a galaxy to match the observed stellar mass versus metallicity relation (MZR) (e.g., Kirby et al. 2013). For instance, Agertz et al. (2020) suggested that the lower-than-expected metallicity compared to observational estimates might be due to overly strong SN feedback that disperses metal-rich gas or the lack of metal enrichment from Pop III stars. The inability of any sub-grid models to reproduce the observed MZR in UFD regime could be due to environmental effects (e.g., tidal stripping) not accounted for in high-resolution simulations, along with other previously mentioned factors. However, Applebaum et al. (2021) argued that there is no environmental difference in the MZR by comparing satellite UFDs and near-field UFDs in MW-like simulations. They predict lower metallicity than the observed MZR at low luminosity ($\lesssim 10^4 L_{\odot}$) and explain this by noting that the timescale for Type Ia SNe is too long, resulting in a delayed release of iron, while star formation quenching occurs too early, leading to stars with low $[\text{Fe}/\text{H}]$ values.

In this study, we explore the impact of IMF sampling on the evolution of UFD analogs using cosmological zoom-in simulations of UFD analogs ($M_{\text{vir}} \approx 10^8 M_{\odot}$) with enhanced resolution, characterized by a gas particle mass of $m_{\text{gas}} \approx 63 M_{\odot}$. We specifically compare the unique properties of the simulated UFD analogs by employing three different IMF sampling techniques: the burst model, stochastic IMF sampling, and individual IMF sampling. In addition, we aim to evaluate how the cosmic metal enrichment histories of the simulated UFD analogs can vary depending on the chosen IMF sampling methods. The paper is organized as follows: In Section 2, we describe the numerical methodology used. In Section 3, we present and discuss the detailed simulation results, focusing on star formation and metal enrichment history, and compare our findings with other relevant studies in Section 4. The main conclusions of this work are summarized in Section 5. Unless otherwise stated, all distances are provided in physical (proper) units for consistency.

Halo	M_{vir}	M_*	$\langle [\text{Fe}/\text{H}] \rangle$	IMF
HALO1-BURST	5.0	10.6	-3.21	BURST
HALO1-SIMF	5.0	14.8	-3.30	SIMF
HALO1-INDIV	5.0	16.1	-2.68	INDIV
HALO2-BURST	8.0	18.6	-3.22	BURST
HALO2-SIMF	8.0	27.3	-3.10	SIMF
HALO2-INDIV	8.0	43.3	-2.20	INDIV
HALO3-BURST	2.0	2.67	-3.14	BURST
HALO3-SIMF	2.0	4.56	-2.66	SIMF
HALO3-INDIV	2.0	1.49	-2.67	INDIV

Table 1. Physical characteristics of the simulated UFD analogs at $z = 0$. Column (1): Run name. Column (2): Virial mass (in units of $10^8 M_{\odot}$ at $z = 0$). Column (3): Stellar mass (in $10^3 M_{\odot}$). Column (4): Average stellar iron-to-hydrogen ratios. Column (5): IMF sampling method.

2 NUMERICAL METHODOLOGY

2.1 Simulation Setup

We carry out a suite of cosmological hydrodynamic zoom-in simulations using a significantly extended version of the N-body smoothed particle hydrodynamics (SPH) code GADGET (Springel et al. 2001; Springel 2005; Schaye et al. 2010). The Λ CDM cosmological parameters used in this study are: a matter density parameter $\Omega_{\text{m}} = 1 - \Omega_{\Lambda} = 0.265$, baryon density $\Omega_{\text{b}} = 0.0448$, present-day Hubble expansion rate $H_0 = 71 \text{ km s}^{-1} \text{ Mpc}^{-1}$, spectral index $n_s = 0.963$, and normalization $\sigma_8 = 0.8$ (Komatsu et al. 2011; Planck Collaboration 2016). We create the initial conditions by running the cosmological initial conditions code MUSIC (Hahn & Abel 2011). Each target halo with a virial mass $M_{\text{vir}} \approx 10^8 M_{\odot}$ at $z = 0$ is identified from a preliminary DM-only simulation carried out with 128^3 particles in a periodic box of linear size $L = 3.125 h^{-1}$ comoving Mpc box. We then apply four consecutive refinements to the target halo region, confined by $3 R_{\text{vir}}$, where R_{vir} is the virial radius at $z = 0$, giving rise to DM and gas masses of $m_{\text{DM}} \approx 500 M_{\odot}$ and $m_{\text{gas}} \approx 63 M_{\odot}$, respectively, in the most refined area. The softening lengths for DM and star particles are fixed $\epsilon_{\text{DM}} \approx 20 \text{ pc}$ at all redshifts. For gas particles, we use an adaptive softening length proportional to the SPH kernel length, with a minimum value of $\epsilon_{\text{gas}, \text{min}} = 2.8 \text{ pc}$.

The baryonic physics employed in this work are similar to those used in Jeon et al. (2017). For detailed descriptions, we refer the reader to that paper, but we provide a brief overview of the critical implementations here. Notably, in this study, we further revise the star formation and SN feedback modules to utilize the stochastic and individual IMF sampling methods, as described in detail in Section 2.3.2 and Section 2.4.2. To investigate the effects of IMF sampling on the evolution of UFD analogs, we perform three sets of comparison simulations. Each pair of runs starts from the same initial condition, targeting one of the UFD analogs (HALO 1, HALO 2, and HALO 3), but adopting three different IMF sampling methods, resulting in a total of nine runs. We designate the runs with burst modeling, stochastic IMF sampling, and individual IMF sampling as BURST, SIMF, and INDIV, respectively. Key physical characteristics of the simulated UFD analogs at $z = 6$ are listed in Table 1.

Name	BURST	SIMF	INDIV
IMF Sampling	Averaged	Stochastic	Individual
Form as	SSP ($500 M_{\odot}$) [0.1 – 100] M_{\odot}	SSP ($500 M_{\odot}$) [0.1 – 100] M_{\odot}	SSP-NoSN ($63 M_{\odot}$) [0.1 – 8] M_{\odot} Individual star [8 – 100] M_{\odot}
Z_*	Uniform	Uniform	Uniform Individual
SN feedback	All at once ($5 \times 10^{51} \text{ erg}$)	Individually (10^{51} erg)	Individually (10^{51} erg)
Delay Time	Immediate	Delayed by lifetime	Immediate
Number of SNE per star particle	5	0 – 10	1

Table 2. Comparison of the properties of the BURST, SIMF, and INDIV methods.

2.2 Chemistry, Cooling and UV background

We solve the coupled, non-equilibrium rate equations for primordial species (H, H^+ , H^- , H_2 , H_2^+ , He, He^+ , He^{++} , e^- , D, D^+ , and HD) at each timestep, accounting for all relevant primordial cooling processes (e.g., H and He collisional ionization, excitation and recombination cooling, bremsstrahlung, inverse Compton cooling, and collisional excitation cooling of H_2 and HD). In addition, we incorporate gas cooling by metal species such as carbon, oxygen, silicon, magnesium, neon, nitrogen, and iron, with cooling rates determined using tables from the photoionization package CLOUDY (Ferland et al. 1998). We also consider the photodissociation of molecular hydrogen (H_2) and deuterated hydrogen (HD) by Lyman-Werner (LW) radiation. To give an effect of reionization, we introduce a cosmic UV background (Haardt & Madau 2012) starting at $z = 7$, and linearly increase its strength until $z = 6$, which corresponds to the expected completion of cosmic reionization (e.g., Gunn & Peterson 1965; Fan et al. 2006).

2.3 Star formation

When the gas density exceeds the critical threshold of $n_{\text{th}} = 100 \text{ cm}^{-3}$, the gas particles become eligible for star formation. According to the Schmidt law (Schmidt 1959), star formation occurs stochastically at a rate described by $\dot{\rho}_* = \rho / \tau_*$, where $\tau_* = \tau_{\text{ff}} / \epsilon_{\text{ff}}$ is the star formation timescale. Here, $\tau_{\text{ff}} = [3\pi / (32G\rho)]^{1/2}$ denotes the free-fall time at a density ρ , and ϵ_{ff} represents the star formation efficiency per free-fall time. In this study, we assume a star formation efficiency of $\epsilon_{\text{ff}} \sim 0.01$ for both Pop III and Pop II stars, which is typical for star formation efficiency in the local Universe (e.g., Leroy et al. 2008). During each numerical timestep Δt , gas is converted into a collisionless star particle only if a randomly generated number between 0 and 1 is less than the smaller of $\Delta t / \tau_*$ and 1. Consequently, the star formation timescale is expressed as:

$$\tau_* = \frac{\tau_{\text{ff}}(n_{\text{H}})}{\epsilon_{\text{ff}}} \sim 400 \text{ Myr} \left(\frac{n_{\text{H}}}{100 \text{ cm}^{-3}} \right)^{-1/2}. \quad (1)$$

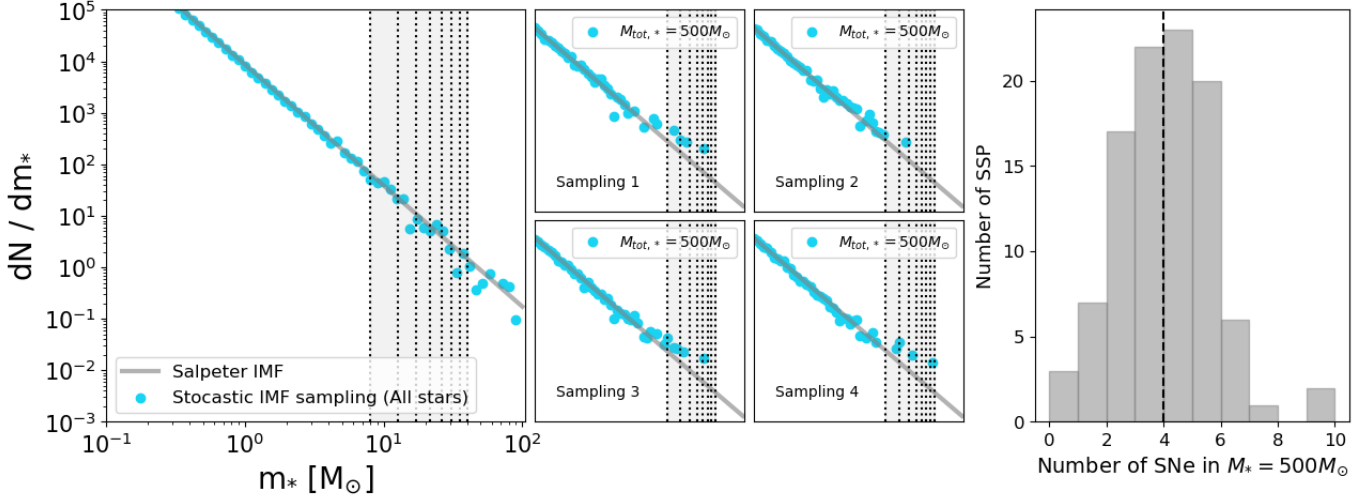


Figure 1. Reconstructed IMF of stars using stochastic IMF sampling. *Left-most panel:* The IMF of all Pop II stars from the HALO1-SIMF run shows good agreement with the assumed Salpeter IMF. For efficient SN modeling (indicated by the gray-shaded region), we store information only for stars within the mass range of $8 - 40 M_{\odot}$, divided into eight logarithmic bins indicated by the vertical dotted lines. *Middle four panels:* Example of star sampling from a single SSP ($m_{\text{PopII}} = 500 M_{\odot}$), illustrating the stochastic nature in the number of Type II SN progenitors. *Right-most panel:* The distribution of the number of SNe within a single Pop II cluster, showing that the typical number of Type II SN progenitor is 4, with the maximum reaching 10.

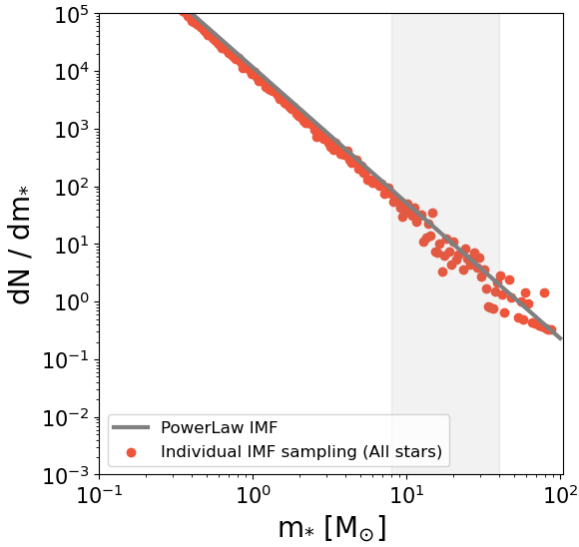


Figure 2. The derived IMF of stars adopting individual IMF sampling. The data from the HALO2-INDIV run, depicted as red circles, shows a strong agreement with the assumed IMF. Similar to the stochastic sampling method, stars within the mass range relevant for Type II SNe are individually tracked to trigger SNe.

2.3.1 Pop III star

It is well known that, due to the lack of metals, Pop III stars typically have masses a few 10 - 100 times greater than those of stars in the present-day Universe (e.g., [Abel et al. 2000](#); [Bromm et al. 2001](#)). However, the exact final masses of Pop III stars are still a matter of ongoing debate (e.g., [Bromm 2013](#); [Hirano et al. 2014, 2015](#); [Klessen & Glover 2023](#)). For instance, [Hirano et al. \(2014\)](#) conducted 2-D hydrodynamic simulations of several hundred cases of Pop III star formation and suggested that their masses could vary significantly, from a few tens of solar masses to $\sim 1000 M_{\odot}$, depending on their

formation environment. In our study, we take advantage of our high mass resolution to represent Pop III stars as individual star particles, unlike the approach in [Jeon et al. \(2017\)](#). However, this work primarily aims to examine how different IMF sampling methods for Pop II stars affect the evolution of UFD analogs. Therefore, to minimize the random effects associated with the mass variability of Pop III stars, we fix the Pop III star mass at $m_{\text{PopIII}} = 20 M_{\odot}$.

2.3.2 Pop II star

Population II (Pop II) stars emerge from gas clouds enriched with metals expelled by earlier Pop III SNe. While the density threshold for Pop II star formation is identical to that of Pop III stars, an additional criterion requires that the gas possesses a metallicity greater than the critical level, $Z_{\text{crit}} = 10^{-5.5} Z_{\odot}$, as suggested by dust-continuum cooling (e.g., [Omukai 2000](#); [Schneider & Omukai 2010](#); [Safranek-Shrader et al. 2016](#)). In both the BURST and SIMF runs, we assume that Pop II stars form as stellar clusters with a mass of $500 M_{\odot}$. Therefore, once a gas particle satisfies the two conditions, n_{th} and Z_{crit} , it is replaced to a sink particle accreting surrounding gas until attaining $m_{\text{PopII}} = 500 M_{\odot}$. Note that when a star particle forms, it inherits the metallicity of the gas from which it was created.

For Pop II stars, we use the Salpeter IMF ([Salpeter 1955](#)), which is defined by the form $dN/d \log m \approx m^{-\alpha}$, with a slope $\alpha = 1.35$ over the mass range of $[0.1 - 100] M_{\odot}$. In the BURST approach, once a Pop II stellar cluster is identified, we treat a star particle as a SSP where stars are continuously distributed according to the given IMF. In SIMF runs, on the other hand, stochastic IMF sampling is performed immediately upon the formation of a Pop II cluster by extracting individual stars from the given IMF. Specifically, we utilize the inverse transform sampling method using the Salpeter IMF as the probability density function. Sampling proceeds until the cumulative mass of the extracted Pop II stars reaches the mass of the stellar cluster, $m_{\text{PopII}} = 500 M_{\odot}$ (e.g., [Haas & Anders 2010](#); [Applebaum et al. 2020](#)). Fig. 1 shows the IMFs of all stars from the HALO1-SIMF run on the left, demonstrating good agreement with the assumed Salpeter IMF. Among the sampled stars, we only retain

information for stars within the mass range of $8 - 40 M_{\odot}$ (indicated as the shaded region in Fig. 1), as these correspond to the masses of Type II SN progenitors (Heger et al. 2003). This mass range is further divided into eight bins, denoted by dotted vertical lines in Fig. 1 for the sake of efficient SN explosion modeling.

We note that, when applying stochastic IMF sampling, the number of Type II SN progenitors from a SSP with $m_{\text{PopII}} = 500 M_{\odot}$ varies due to randomness. This variability is illustrated in the four middle small panels of Fig. 1. For instance, in the first sampling shown in Fig. 1, there are 4 Type II SN progenitors, while in the second sampling, the number drops to 2. The rightmost panel of Fig. 1 presents a histogram of the number of SNe in the SSP. It reveals that the typical number of Type II progenitors turns out to be 4 for a single Pop II cluster ($m_{\text{PopII}} = 500 M_{\odot}$), and the maximum number of stored stars can reach 10. In an extreme case, there could be no progenitors, meaning the star cluster would experience no Type II SN events.

In the individual sampling method, when a gas particle meets the conditions to form Pop II stars, it is converted into a sink particle with a mass of $m_{\text{PopII}} = 63 M_{\odot}$, and star masses are then sampled randomly from the range $0.1 - 100 M_{\odot}$ according to the Salpeter IMF. If stars with masses between $0.1 M_{\odot}$ and $8 M_{\odot}$ are sampled, the process continues until the total mass reaches $63 M_{\odot}$. At this point, sampling stops, and the collection is regarded as an SSP particle, with no massive stars exceeding $8 M_{\odot}$. Conversely, if the mass of a sampled star falls within the range of $8 - 100 M_{\odot}$, we regard a sink particle as an individual star. Stars with masses of $8 - 40 M_{\odot}$ are designated as Type II SN progenitors, while those of $40 - 100 M_{\odot}$ are assumed to directly collapse into black holes (BHs) without exerting feedback. In this method, massive stars collapse into SNe or BHs, and only SSP particles contribute to the stellar mass.

Fig. 2 demonstrates that the IMF of sampled stars in the HALO2-INDIV run matches well with the assumed Salpeter IMF. Unlike the BURST and SIMF methods, stars in the INDIV run—comprising $63 M_{\odot}$ SSP stars—exhibit more diverse stellar metallicities. This smaller SSP mass, coupled with discrete SN feedback from massive individual stars, better captures variations in star formation. On the contrary, stars within an SSP in the BURST and SIMF runs, which involve a relatively large mass of stars ($500 M_{\odot}$), all share the same metallicity, making them less effective at representing the dynamics of star formation. Table 2 provides a summarized comparison of the three methods: BURST, SIMF, and INDIV.

2.4 Stellar feedback

During a SN explosion, energy is transferred as thermal energy to the nearest gas particles, significantly increasing their temperature to levels exceeding $T = 10^6 - 10^8$ K. However, this energy can quickly dissipate if the numerical resolution is inadequate for accurately modeling the evolution of SN ejecta (e.g., Stinson et al. 2007). To tackle this well-known overcooling issue, we adopt the numerical method proposed by Dalla Vecchia & Schaye (2012), which reduces the number of neighboring gas particles to achieve a temperature increase of $\Delta T > 10^{7.5}$ K, a necessary condition for effective SN feedback. Moreover, we utilize a timestep limiter and adjust the timestep to ensure that the ratio of the surrounding SPH particles does not exceed 4 (e.g., Saitoh & Makino 2009), allowing the gas particles to respond appropriately to the sudden input of SN energy (e.g., Dalla Vecchia & Schaye 2012).

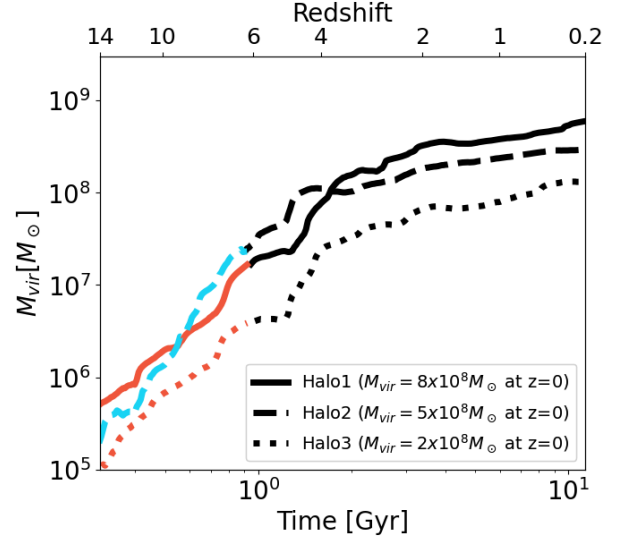


Figure 3. Dark matter assembly histories of the simulated UFD analogs. Initially, all haloes begin as minihaloes with masses around $M_{\text{halo}} \approx 10^5 M_{\odot}$ at redshifts $z \geq 14$. Then, they gradually grow to reach masses of about $M_{\text{halo}} \approx 10^8 M_{\odot}$ by redshift $z = 0$.

2.4.1 Pop III stars

The ultimate fates of Pop III stars are primarily determined by their initial mass (e.g., Heger & Woosley 2010; Yoon et al. 2012). For example, metal-free stars with masses ranging from $10 M_{\odot} \lesssim m_* \lesssim 40 M_{\odot}$ are anticipated to undergo conventional core-collapse supernovae (CCSNe), whereas those with masses between $140 M_{\odot}$ and $260 M_{\odot}$ are likely to result in pair-instability supernovae (PISNe). In this study, with the fixed mass of Pop III stars set at $m_{\text{Pop III}} = 20 M_{\odot}$, the SN explosion energy for an individual Pop III star is established at $E_{\text{CCSN}} = 10^{51}$ erg for a CCSN. Also, we utilize the metal yields of Pop III SNe provided by Heger & Woosley (2002, 2010). Given that the mass resolution of this work is high enough to represent an individual massive Pop III star, the SN explosion and the release of metals are treated as a single event whenever a Pop III SN is triggered.

2.4.2 Pop II stars

For the stellar feedback associated with Pop II stars, we consider conventional Type II SN, Type Ia SN, and Asymptotic Giant Branch (AGB) feedback. However, the most critical factor influencing the evolution of UFDs might be the Type II SNe from massive Pop II stars. As previously mentioned, this study seeks to examine whether the evolution of UFD analogs can vary depending on the IMF sampling method employed. To address this question, we use three distinct approaches for Type II SN explosion.

First, under the BURST approach, the total energy from SNe is released simultaneously into the surrounding medium during simulations. This method has been employed in our previous studies (e.g., Jeon et al. 2017, 2021a,b). We define the energy of a single SN as $E_{\text{SN,single}} = 10^{51}$ erg. Therefore, the total energy is calculated as $E_{\text{SN,total}} = N_{\text{SN}} \times E_{\text{SN,single}}$, where N_{SN} represents the IMF-averaged number of Type II SN progenitors, about 5 when using the Salpeter IMF. As a result, $E_{\text{SN,total}} = 5 \times 10^{51}$ erg is deposited each time a Pop II SSP forms in the BURST run. The metal yields from these SN events are also averaged according to the IMF and released simultaneously, based on metallicity-dependent yield tables (Porti-

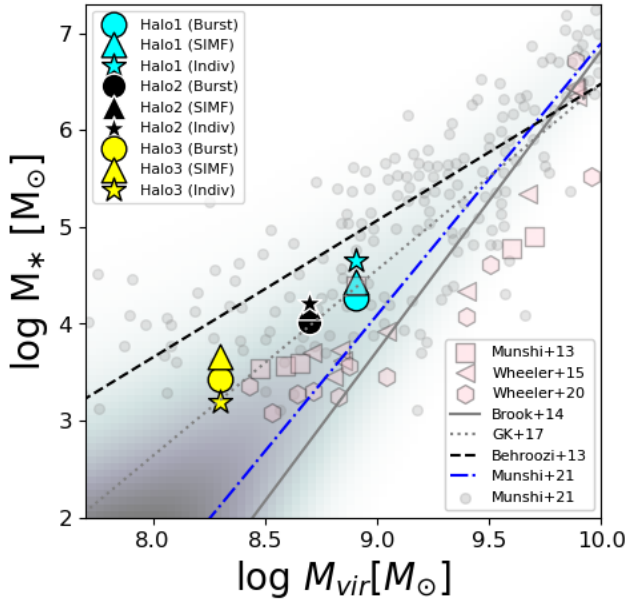


Figure 4. The relationship between stellar mass and virial mass is depicted for three simulated galaxies, utilizing three distinct IMF sampling methods. These methods are represented by different symbols: circles for the BURST runs, triangles for the SIMF runs, and stars for the INDIV runs. Generally, the stellar mass estimates in the INDIV runs are higher compared to those in the BURST and SIMF runs for HALO1 and HALO2, whereas this pattern is reversed for HALO3.

nari et al. 1998). It is important to note that, due to the absence of photoionization heating by stars, the thermal energy and metals from the SN events are designed to be deposited immediately after the formation of Pop II stars. This approach prevents the overproduction of stars during their main-sequence phase.

Secondly, in simulations with stochastic IMF sampling, SN energy is released through discrete events rather than all at once. As detailed in Section 2.3.2, after randomly sampling Pop II stars from a specified IMF, we retain only the information of massive stars, categorized into eight mass bins. If the age of a selected star surpasses the main-sequence lifetime of its progenitor, a CCSN event is triggered, releasing thermal energy and metals into the surrounding gas particles. Consequently, multiple SN explosions can occur individually within a single stellar cluster, starting with the explosion of the most massive Type II SN progenitor. Each SN releases an energy of $E_{\text{SN, single}} = 10^{51}$ erg. The lifetime and stellar yields of each progenitor are calculated based on their mass and metallicity, using the information of the high-mass star previously stored through IMF sampling (Portinari et al. 1998).

Thirdly, using individual IMF sampling, a Type II SN event happens whenever an individual massive Pop II star ($8 - 40 M_{\odot}$) forms, releasing an energy of $E_{\text{SN, single}} = 10^{51}$ erg along with corresponding metals into the ISM. Unlike the BURST and SIMF methods, which typically result in 4-5 SN events from a single SSP when Pop II star formation takes place, this individual sampling approach allows prior explosions to regulate star formation more consistently, determining whether subsequent explosions will occur. This means that, although the SIMF method also considers individual SN explosions, multiple events are set to occur regardless of whether the surrounding medium has already been regulated.

Intermediate-mass stars, with masses ranging from $0.8 M_{\odot}$ to $8 M_{\odot}$, shed mass during their AGB phase. We use the tables from

Marigo (2001) to calculate the metal yields from these Pop II stars at each timestep, releasing metals into the surrounding medium. For Type Ia SNe, which stem from progenitors with masses ranging from $3 M_{\odot}$ to $8 M_{\odot}$, we utilize empirical delay time distributions (e.g., Barris & Tonry 2006; Förster et al. 2006) and derive metal yields using the spherically symmetric "W7" model (Thielemann et al. 2003). The energy released by Type Ia SN is imparted as thermal energy to nearby gas particles, though its feedback is relatively weak since the energy is injected gradually over billions of years. Metals expelled from AGB stars and SNe are evenly distributed among 32 neighboring gas particles, resulting in a metallicity Z_i for each gas particle, where $Z_i = m_{\text{metal},i} / (m_{\text{gas}} + m_{\text{metal},i})$. Metal transport is carried out through a diffusion scheme, with mixing efficiency on unresolved scales determined by the physical properties at the SPH smoothing kernel scale (e.g., Klessen & Lin 2003; Greif et al. 2009).

3 RESULTS

This section presents the key findings from our series of simulations. In particular, Section 3.1 investigates how various IMF sampling methods influence both the burstiness of star formation and the resulting SFHs of the simulated UFD analogs. Section 3.2 analyzes the effects of different IMF sampling methods on the resulting metallicity, focusing on the MDF and the MZR.

3.1 Mass assembly history

As shown in Fig. 3, each target halo starts as a minihalo with a virial mass of $M_{\text{vir}} = [1 \sim 8] \times 10^5 M_{\odot}$ at $z \gtrsim 14$. These haloes eventually evolve into galaxies with a total mass of $M_{\text{vir}} = [2 \sim 8] \times 10^8 M_{\odot}$ and a stellar mass of $M_* \approx 10^3 - 10^4 M_{\odot}$ at $z = 0$. Here, we only present the mass assembly histories of galaxies in BURST runs, as those from the SIMF and INDIV runs are identical. It should be mentioned that we conduct our runs until $z \approx 6$, by which time star formation in these small galaxies ($M_{\text{vir}} \lesssim 10^9 M_{\odot}$ at $z = 0$) tends to cease due to global heating from reionization and internal feedback (e.g., Jeon et al. 2017, 2021a). Despite the absence of hydrodynamic simulations down to redshift $z = 0$, we can utilize data from DM-only simulations that reach $z = 0$ with the same initial conditions. This enables us to identify the progenitor halos at $z = 6$ for the final assembled halo at $z = 0$ in hydrodynamic simulations. Assuming that star formation has already ceased in all progenitor haloes prior to $z = 6$, we identify which stars, formed before $z = 6$, have become members of the final halo at $z = 0$.

To achieve this, we first employ DM-only simulations. Specifically, we identify the progenitor haloes at $z = 6$ that share more than 80% of their DM particle IDs with those of the final halo at $z = 0$. Next, we match the progenitor haloes at $z = 6$ from the DM-only simulations with those from the hydrodynamic runs. This involves using the central positions and virial radii of the progenitor haloes identified at $z = 6$ from the DM-only simulations to locate the corresponding haloes in the hydrodynamic runs. During this process, we confirm that an almost 100% match of the haloes can be achieved. Finally, we analyze the star particles within the progenitor haloes identified in the hydrodynamic runs, as these stars represent the member stars of the final halo at $z = 0$.

The derived stellar masses of the UFD analogs at $z = 0$ are presented in Fig. 4 as a function of their virial masses at $z = 0$, illustrating the stellar mass-halo mass relation (SMHM), with the precise values detailed in Table 1. An increasing trend in stellar masses is found with increasing halo masses. The three runs, which adopt the same

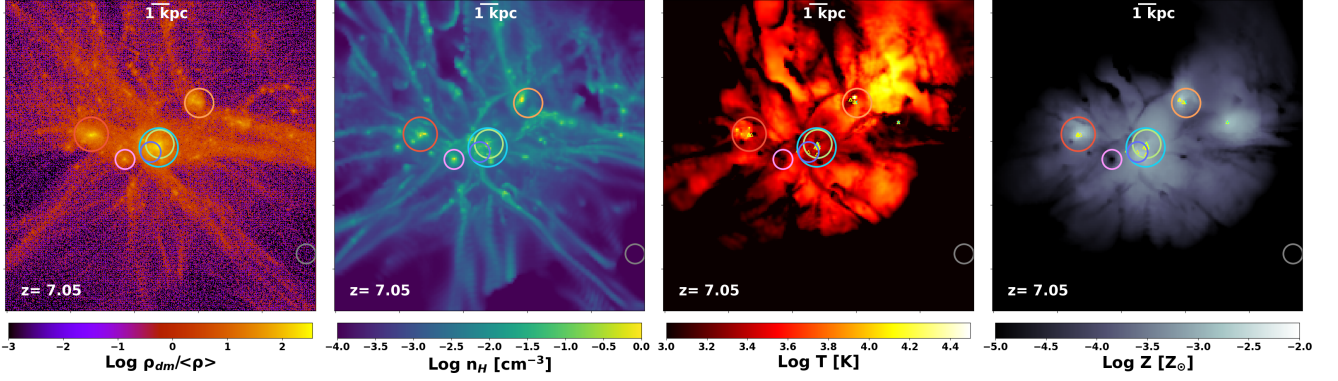


Figure 5. The morphology of the simulated UFD analog for HALO2 at $z \approx 7$ is illustrated. From left to right, the panels show dark matter overdensity, hydrogen number density, gas temperature, and gas metallicity, respectively, averaged along the line of sight within a cubical region of 80 kpc comoving size for the BURST. Colored circles indicate the virial radii of the progenitor haloes. The visualization clearly demonstrates that star formation occurs in multiple progenitor haloes rather than predominantly in the most massive main progenitor halo. This is attributed to the high resolution of our simulations, which enables the tracing of star formation from Pop III stars in minihaloes with masses $M_{\text{vir}} \approx 10^{5-6} M_{\odot}$ at $z > 14$.

initial conditions but employ different IMF sampling methods, are distinguished by different symbols. The resultant stellar masses range from $M_* \approx 1.49 \times 10^3 M_{\odot}$ to $M_* \approx 4.33 \times 10^4 M_{\odot}$ at $z = 0$. Since we halt our simulations at $z = 6$, the stellar masses at $z = 6$ may differ from the final masses at $z = 0$ due to mass loss from stellar particles during the AGB phase and Type Ia SNe. To estimate the final stellar masses at $z = 0$, we calculate the mass loss of all stellar particles based on the assumed IMF, with a specific focus on the BURST runs. For the SIMF and INDIV cases, we primarily consider mass loss during the AGB phase, as the metals from Type II SN events are released immediately within approximately 40 Myr, the lifetime of an $m_{\text{popII}} = 8 M_{\odot}$ star, which is usually shorter than the simulated period. These mass loss estimates are validated by comparing them with results from selected hydrodynamic simulations that perform down to $z = 0$.

As shown in Fig. 4, we find that the stellar masses of the INDIV runs are likely to be larger than those in the BURST (SIMF) runs by 132%(58%) and 51%(8%) for HALO 1 and HALO 2, respectively. However, this pattern is reversed in the HALO3 case. This trend will be discussed in detail in Section 3.1.1. Also, we compare our SMHM relationship estimates with the best-fit results from previous abundance-matching studies (e.g., Behroozi et al. 2013; Brook et al. 2014; Garrison-Kimmel et al. 2017; Munshi et al. 2021) and simulated values from other theoretical works (e.g., Munshi et al. 2013; Wheeler et al. 2015, 2019; Munshi et al. 2021). Notably, Munshi et al. (2021) predicted a steeper slope in the UFD regime, represented by the blue dash-dot line, where the fit is based on other simulated results shown as gray circles in Fig. 4. They assumed an increasing scatter in the SMHM relationship as one moves to lower mass regimes, compared to the fits from the abundance-matching approach using smaller scatter. Our results lie between these fits, which are based on varying assumptions regarding the level of scatter.

3.1.1 The evolution of the progenitor haloes

As we trace the star formation activity within minihaloes at high- z , our findings reveal that star formation commences across multiple progenitor haloes, rather than being predominantly concentrated in the most massive main progenitor halo. Fig. 5 illustrates the distribution of progenitor haloes of HALO2 at $z \approx 7$, with each progenitor

halo represented by circles of different colors. These haloes eventually merge into a single UFD analog at $z = 0$. Each panel, from left to right, presents the DM overdensity, hydrogen number density, gas temperature, and gas metallicity, averaged along the line of sight, within a cubical region of comoving size ~ 80 kpc. The presence of multiple progenitor haloes implies that the member stars of the UFD analog at $z = 0$ originate from diverse environments within each progenitor, rather than undergoing a monolithic evolution in a single main progenitor halo. Consequently, the characteristics of these stars are determined by the specific star formations and metal enrichment histories they experienced within their respective progenitor haloes.

Fig. 6 shows the SMHM relations for each progenitor haloes at $z = 6$ in HALO1, HALO2, and HALO3, generally demonstrating an upward trend in stellar mass with increasing halo mass. However, the precise stellar masses vary depending on the sampling method, typically yielding higher stellar masses in the INDIV runs compared to the BURST and SIMF cases, especially at relatively massive progenitor halo ($M_{\text{vir,ph}} \gtrsim 10^7 M_{\odot}$ at $z = 6$). The stellar masses are calculated by summing the values of the star particles within the virial radius of each progenitor halo at $z = 6$. The order of the progenitors is arranged from the most massive (PH0) to the least massive haloes (PH7), specifically, at $z = 6$, thus this does not imply that PH0 is always the most massive during $z \geq 6$.

The detailed evolution of each progenitor haloes of HALO1 is displayed in Fig. 7, with results shown from left to right for the BURST, SIMF, and INDIV runs, each adopting different IMF sampling methods. The top panels depict the evolution of DM (solid line), gas (dotted line), and stellar (dashed line) masses, respectively, while the bottom panels represent the corresponding metallicity of star particles, denoted as $[\text{Fe}/\text{H}]$, formed in each progenitor haloes. The open circles in the bottom panels, sharing the same color, indicate stars that originated in different haloes other than the selected progenitors but eventually merged into one of these progenitor haloes. In addition, the size of the circles indicates the relative mass of the progenitor halo at the time those stars entered the progenitor haloes. Since we compare runs with identical initial conditions but different IMF sampling methods, the DM evolution of each progenitor halo remains consistent across the three cases. However, the gas and stellar evolution vary depending on the star sampling approach and the associated feedback effects. Generally, it shows that most progeni-

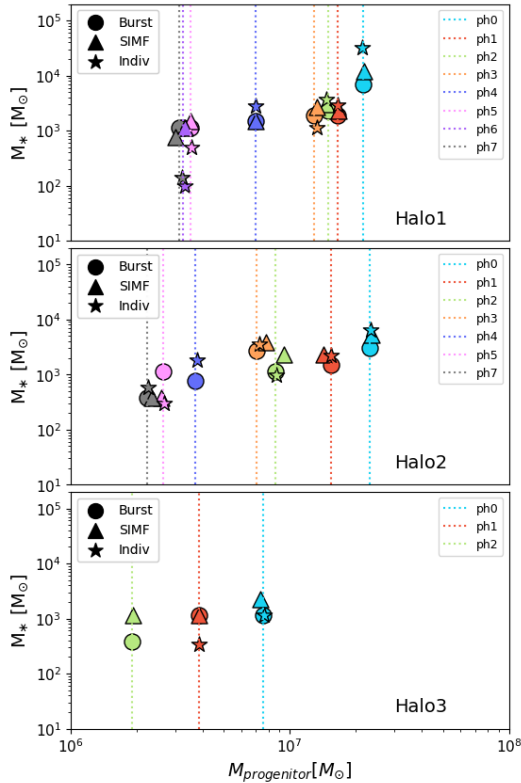


Figure 6. The relationship between stellar and virial masses within progenitor haloes at $z = 6$, which eventually assemble into a single UFD analog by $z = 0$. There is a tendency for massive progenitor haloes to have higher stellar masses in the INDIV runs compared to the BURST and SIMF runs. Conversely, in smaller haloes, this trend is reversed. This occurs because, in massive haloes, when SNe explode individually in the INDIV runs, the weaker feedback effect allows for continuous star formation over a relatively long duration. However, in low-mass haloes, star formation occurs very late, and the reionization effect leads to only 1-2 starbursts. Consequently, the formation of 1-2 individual SNe suppresses further star formation, giving rise to a lower total stellar mass.

tor haloes experience a gas loss of 1-2 orders of magnitude between $z = 7$ and $z = 6$, during which the effect of reionization is introduced.

3.1.2 Burst vs. stochastic IMF sampling

In this section, we present a comparative analysis of the simulation results for two scenarios: BURST, where multiple SNe are triggered simultaneously, and SIMF, where SN events are staggered based on the lifetimes of massive stars. It is important to note that in the BURST scenario, the number of SNe within a SSP with a mass of $m_{\text{PopII}} = 500 M_{\odot}$ is fixed, whereas, in SIMF, this number varies due to stochastic effects. Overall, we find that star formation tends to occur more continuously in the SIMF scenario compared to BURST.

In the most massive progenitor halo, PH0, denoted by cyan lines and circles in Fig. 7, there are two starburst periods, from $z = 9.2$ to $z = 8.6$ and from $z = 7.4$ to $z = 6.0$ for both runs. As the halo mass increases in the later stages, the difference in feedback effects becomes more pronounced. For instance, between $z = 7.4$ and $z = 6.0$, about 2.3 times more stars are formed in the SIMF case. This is because the staggered SN explosions in the SIMF run make it difficult to sufficiently reduce the gas density, allowing continuous star formation, unlike the BURST run. Consequently, the SIMF run produces stars

with a maximum metallicity of $[\text{Fe}/\text{H}] = -2.0$, whereas the BURST run shows stars with a maximum metallicity of $[\text{Fe}/\text{H}] = -2.3$.

In PH1, colored red in Fig. 7, after the initial starburst at $z \approx 10.3$ in both the BURST and SIMF runs, subsequent in-situ star formation is delayed until $z = 7$ in the BURST scenario. Meanwhile, in the SIMF run, the gas density recovers, allowing star formation to resume at $z = 7.8$. This occurs because, in the SIMF scenario, only two stochastically sampled stars are capable of exploding as SNe in the initial SSP particle, resulting in a weaker feedback effect compared to the initial starburst at $z = 10.3$ in the BURST run. For the case of PH2, shown in green, although it ranks as the third most massive halo at $z \approx 6$, its virial mass surpasses others at $z \geq 9$, allowing it to be the first to initiate star formation at $z \approx 16$. Interestingly, in PH2, we find that the initial in-situ star particles at $z \approx 11.3$ have significantly low-metallicities of $[\text{Fe}/\text{H}] = -5.5$ in the BURST run and $[\text{Fe}/\text{H}] = -4.8$ in the SIMF run. This is due to external metal enrichment as follows: at $z = 15.7$, metals are ejected by Pop III and Pop II stars, represented by open circles, formed at a density peak about 1 kpc away, beyond the virial radius of PH2 ($r_{\text{vir}} \approx 200$ pc). Over the next 150 Myr, these externally sourced metals enrich the gas within the virial radius of PH2, leading to the formation of metal-poor Pop II stars with $[\text{Fe}/\text{H}] \lesssim -4.8$ in PH2.

In the relatively low-mass progenitors ($M_{\text{vir}} \lesssim 6 \times 10^6 M_{\odot}$ at $z = 6$), randomness increases due to the small number of star particles formed. This is because star formation not only begins later but is also likely to be quickly quenched by the reionization effect. For example, in PH5, star formation begins at $z = 6.74$ and lasts for a very brief period until $z = 6.59$. Intriguingly, in PH7, star formation begins early at $z \approx 11$ since it was the second most massive halo at that time. However, it hardly increases in halo mass, forming only a single in-situ star particle in the BURST run, whereas $M_{*,\text{PopII}} = 1000 M_{\odot}$ stars are formed due to weaker SN feedback in the SIMF run. Despite this, the final stellar mass of BURST surpasses that of SIMF because of the contribution from merged stars in the BURST run.

From this point onward, the discussion focuses on comparing the BURST and SIMF runs of HALO2, as illustrated in Fig. 8. In the BURST run of HALO2, the most massive progenitor halo, PH0, denoted in cyan in Fig. 8, initiates in-situ star formation relatively late at $z \approx 8.5$. Note that these stars are Pop II stars formed through external metal enrichment. The metals originate from a density peak beyond the virial radius of PH0, giving rise to the formation of metal-poor Pop II stars with $[\text{Fe}/\text{H}] = -4.3$. During star formation at $z \approx 8.5$ in the PH0 progenitor halo, the BURST run produces a SSP with a mass of $M_{*,\text{PopII}} = 500 M_{\odot}$. In contrast, the SIMF run results in a starburst at the same redshift, forming $M_{*,\text{PopII}} = 2500 M_{\odot}$ of stars. This discrepancy arises because, in the BURST run, 5 SNe explode all at once, immediately suppressing subsequent star formation. On the other hand, in the SIMF run, the initial SN explosion with $E_{\text{SN}} = 10^{51}$ erg has a weaker feedback effect, failing to immediately inhibit star formation, thus allowing for continuous star formation. Similar to the BURST run, the very first in-situ star in the SIMF run, formed via external metal enrichment, exhibits low-metallicity of $[\text{Fe}/\text{H}] = -4.7$, while the subsequently formed stars show enhanced metallicity, ranging from $[\text{Fe}/\text{H}] = -2.6$ to -2.2 .

Although PH1, shown in red in Fig. 8, is the second most massive progenitor at $z = 6$, it was the most massive halo at $z \approx 15$, commencing star formation at $z \approx 12.5$ in the BURST run. Unlike PH0, the metallicity floor in PH1 is set by in-situ Pop III stars, resulting in Pop II stars with $[\text{Fe}/\text{H}] = -3.2$. Both the BURST and SIMF runs produce the same amount of Pop II stars ($M_{*,\text{PopII}} = 1000 M_{\odot}$) from the initial starburst. However, the delay time for the subsequent starburst differs: $\Delta t \sim 340$ Myr for SIMF and $\Delta t \sim 150$ Myr for BURST.

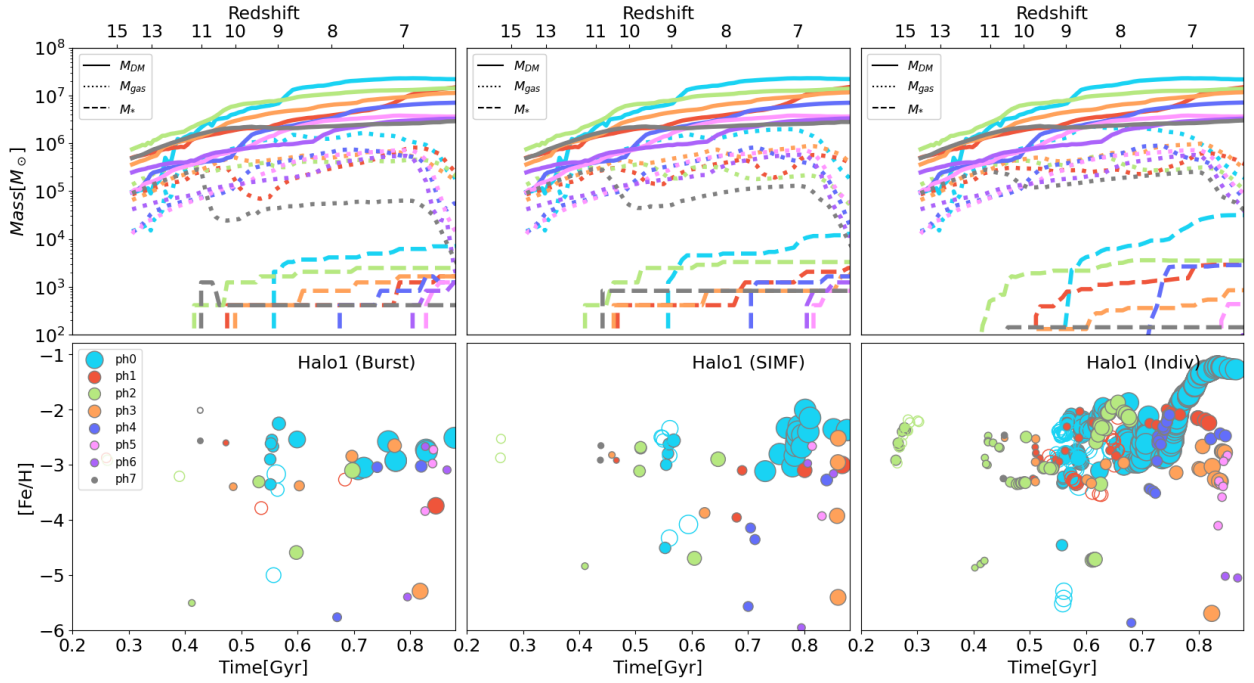


Figure 7. The top panels illustrate the evolution histories, while the bottom panels show the corresponding metallicity of star particles within progenitor haloes identified at $z \approx 6$ for HALO1, utilizing different IMF sampling methods: BURST (left), SIMF (middle), and INDIV (right). In the top panels, solid, dotted, and dashed lines represent the evolution of dark matter, gas, and stars, respectively. In the bottom panels, we differentiate between stars formed through in-situ star formation within the virial radius (filled circles) and those that merged after being generated in other progenitor haloes (open circles). Notably, star formation is more continuous in the INDIV run compared to the BURST and SIMF cases, where each event produces $500 M_{\odot}$ of stars followed by multiple SN explosions. In the INDIV run, SNe explode individually, allowing for immediate decisions on subsequent star formation. Also, the energy from a single SN is insufficient to suppress further star formation, particularly in more massive haloes, leading to consecutive star formation.

This difference is due to the occurrence of 10 SN explosions in the SIMF run, compared to 8 SNe in the BURST run. After the second starburst, stars continue to form until $z = 6$ in the SIMF, while there is no further in-situ star formation in the BURST run, leading to 50% more stellar mass in the SIMF run. A similar trend is found in PH2, giving rise to 66% more stellar mass in the SIMF run.

For PH3, star formation occurs in two distinct periods, $z = 8.1 - 7.6$ and $z = 6.7 - 6.4$, in the BURST run, whereas in the SIMF run, stars form continuously from $z = 8.6$ to $z = 6.5$. Meanwhile, similar to HALO1, in low-mass haloes ($M_{\text{vir}} \lesssim 6 \times 10^6 M_{\odot}$ at $z = 6$), star formation begins late, at $z \gtrsim 7.5$. We find that low-metallicity stars with $[\text{Fe}/\text{H}] \lesssim -5$, as seen in PH4 and PH5, arise from external metal enrichment. As the progenitor halo mass decreases and the number of stars diminishes, random effects become more significant. Also, the reionization effect takes place shortly after star formation, combining with stellar feedback effects, resulting in similar final stellar masses in both the BURST and SIMF runs.

3.1.3 stochastic IMF sampling vs. individual method

As detailed in Section 2.3.2 and 2.4.2, massive Pop II stars, which can explode as SNe, are individually sampled in INDIV runs. By contrast, stars form as a SSP particle with a mass of $m_{\text{PopII}} = 500 M_{\odot}$ in SIMF runs. The middle and right panels of Fig. 7 and Fig. 8 show that star formation tends to be more continuous in INDIV runs compared to SIMF runs. In both scenarios, a SN explodes with the same energy of 10^{51} erg. However, if gas suppression does not occur with the first SN, the SIMF run will generate another SSP with $m_{\text{PopII}} = 500 M_{\odot}$ before additional SNe from the previous SSP, leading to rapid increases in

stellar masses, followed by a strong feedback effect from multiple SSPs. On the other hand, the INDIV run will gradually form stars, producing $63 M_{\odot}$ at a time. An advantage of the INDIV runs is that stars are represented by an SSP with a smaller mass compared to those in the BURST and SIMF runs. This enables stars to form from gas enriched by metals from earlier SNe, allowing them to more accurately reflect the immediate changes in gas metallicity.

In the case of PH0 in HALO1, shown in the rightmost panel of Fig. 7, unlike the SIMF scenario with two major starburst periods at $z = 9.2 - 8.6$ and $z = 7.4 - 6.0$, stars form continuously in the INDIV run, reaching a maximum metallicity of $[\text{Fe}/\text{H}] = -1.21$. Consequently, the final stellar mass in INDIV is about three times larger than in SIMF. In PH1 of the SIMF run, there is an ~ 200 Myr delay until the next star formation at $z \approx 7.8$ after the first in-situ star formation at $z \approx 10.3$. Meanwhile, stars form continuously in PH1 of the INDIV run. Intriguingly, the presence of this delay in the SIMF run allows metals to diffuse, resulting in stars formed at $z \lesssim 7.8$ having lower metallicity ($[\text{Fe}/\text{H}] \lesssim -3.1$) compared to those formed at $z \approx 10.3$ ($[\text{Fe}/\text{H}] \approx -2.9$). On the other hand, as the gas metallicity gradually increases in the INDIV run, the average stellar metallicity in PH1 reaches $[\text{Fe}/\text{H}] \approx -2.05$. This trend, where star particles form continuously and the associated metallicity increases linearly, is consistently found across all progenitor haloes from PH2 to PH4.

For low-mass progenitor haloes, however, such as PH5, PH6, and PH7 of HALO1, there is a trend opposite to that of the massive progenitor haloes, showing a higher final stellar mass in SIMF compared to INDIV. For instance, in PH6, three SSP particles in SIMF are formed before starting at $z \approx 6.9$, with only the initial SNe being triggered at a given time. Subsequent SN explosion effects are ineffective since star for-

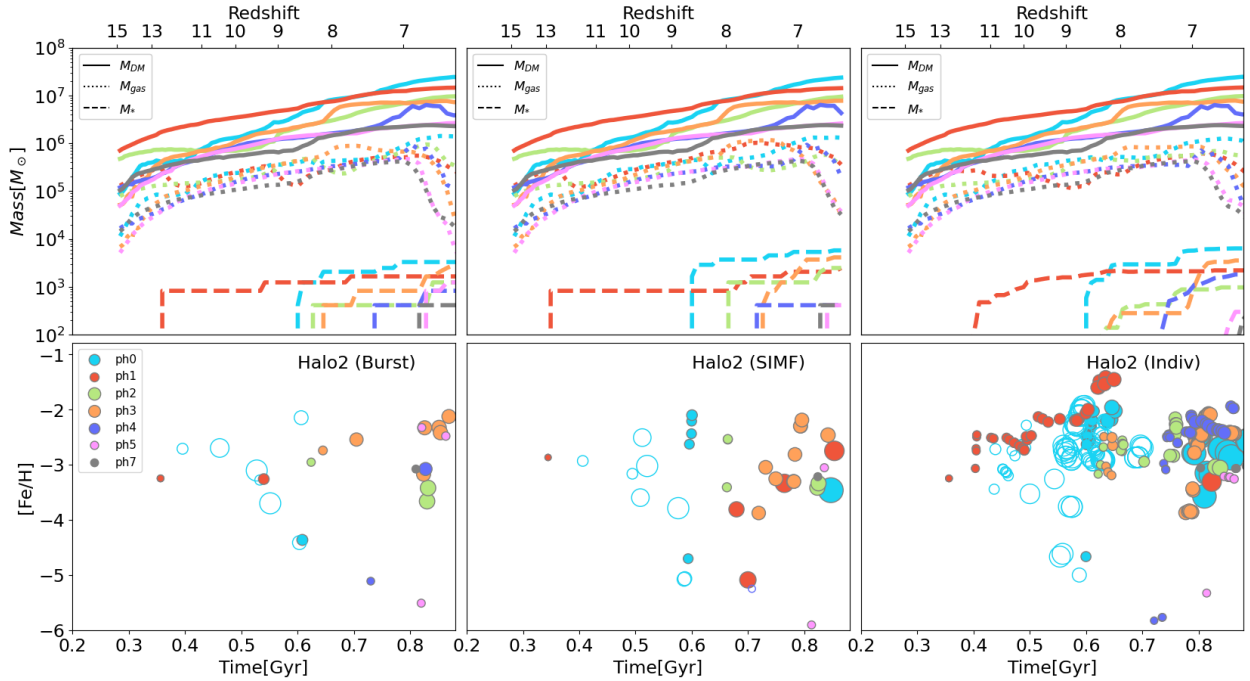


Figure 8. The same as Fig. 7, but for HALO2. Since HALO2 ($M_{\text{vir}} \approx 5 \times 10^8 M_{\odot}$ at $z = 0$) is less massive than HALO1 ($M_{\text{vir}} \approx 8 \times 10^8 M_{\odot}$ at $z = 0$), star formation in each progenitor halo generally begins later. A similar trend to HALO1 is observed, with star formation being more continuous in the order of BURST, SIMF, and INDIV runs.

mation has already been quenched due to the combined effects of the first SN feedback and reionization. Meanwhile, in the INDIV run, only a single SN from a star at $z \approx 6.4$ occurs, which is sufficient to suppress further star formation thanks to the additional reionization effect. This results in a total stellar mass of $M_* \approx 97 M_{\odot}$ in the INDIV run, which is significantly smaller than the $M_* \approx 1.1 \times 10^3 M_{\odot}$ achieved in the SIMF run. In other words, in small progenitor haloes, 1-2 SNe are enough to halt star formation. However, in the SIMF runs, where star formation occurs in the form of SSPs, the delayed SN effect leads to an overproduction of stellar mass in these small progenitors.

Here, we compare the two scenarios in HALO2, which exhibit a trend similar to HALO1. For example, in the SIMF run, PH1 shows a delay of about 340 Myr after the initial star formation, whereas in the INDIV run, continuous star formation occurs for 300 Myr until $z = 8.5$. As a result, stars with a maximum metallicity of $[\text{Fe}/\text{H}] = -1.41$ form in the INDIV runs, while the maximum metallicity in the SIMF run only reaches $[\text{Fe}/\text{H}] = -2.75$. As expected, the difference in the final stellar masses in progenitor haloes between the two scenarios depends on their progenitor mass ranges. Notably, in the most massive progenitor halo, PH0 of HALO2 ($M_{\text{vir}} \approx 2.35 \times 10^7 M_{\odot}$ at $z \approx 6$), the stellar mass in the INDIV run is about 22% higher than in the SIMF run. This is significant because PH0 contributes 42% to the total stellar mass of all stars formed in all progenitor haloes of HALO2. However, in the progenitor mass range from $M_{\text{vir}} = 7.2 \times 10^6 M_{\odot}$ to $1.5 \times 10^7 M_{\odot}$, the final stellar masses between the two scenarios are similar. Specifically, the stellar masses differ by factors of 1.0, 2.3, and 1.0 for PH1, PH2, and PH3, respectively, in HALO2.

For low-mass progenitor haloes, a similar trend to HALO1 is observed, with higher final stellar mass in the SIMF run compared to the INDIV run. For instance, in the case of PH5, star formation begins very late ($z \approx 6.7$). Here, stars formed, due to external metal enrichment, show low-metallicities ($[\text{Fe}/\text{H}] \lesssim -5.3$) in both runs. In the

SIMF run, a SSP particle with an initial mass of $500 M_{\odot}$ is created, and no additional stars form due to SN feedback combined with the reionization effect. On the other hand, in the INDIV run, subsequent stars with $[\text{Fe}/\text{H}] = -3.2$ form at $z \lesssim 6.5$. Despite this extended star formation, the SIMF run results in a higher final stellar mass of $M_* = 380 M_{\odot}$ compared to $M_* = 290 M_{\odot}$ in the INDIV run, due to the formation of stars in larger mass units ($500 M_{\odot}$) in the SIMF run.

3.1.4 Star formation histories and burstiness

So far, we have examined how stars form within UFD analogs according to the IMF sampling method, demonstrating that stars originate from multiple progenitor haloes rather than a single main progenitor. Fig. 9 depicts total star formation rates (SFRs), with each progenitor halo denoted by different colors. The panels, from top to bottom, show SFRs for the BURST, SIMF, and INDIV runs for HALO1. The SFRs, computed in 3.5 Myr time bins, range from $10^{-6} M_{\odot}/\text{yr}$ to a few $10^{-4} M_{\odot}/\text{yr}$. We find that SFRs from the BURST and SIMF runs are likely to be bursty, while star formation is more continuous in the INDIV runs, particularly in relatively massive progenitor haloes ($M_{\text{vir}} \gtrsim$ a few $10^7 M_{\odot}$ at $z \approx 6$).

As star formation becomes more bursty, the intervals between starbursts increase, leading to extended periods without new star formation. To quantify this, we calculate the quenched period fraction. For example, Fig. 10 illustrates the SFRs taken from one of the progenitor haloes, PH0, as depicted in Fig. 9. We sum the periods during which no stars are formed (shaded regions) and divide this by the total star formation period, defined as the time from the first to the last star formation event in each progenitor halo. From this definition, the resulting fraction is about 15.7% for PH0 in the INDIV run for HALO1.

Fig. 11 displays the quenched period fractions for all progenitor haloes in HALO1 (left panel) and HALO2 (right panel). These results show that in the INDIV runs, the quenched period fraction ranges

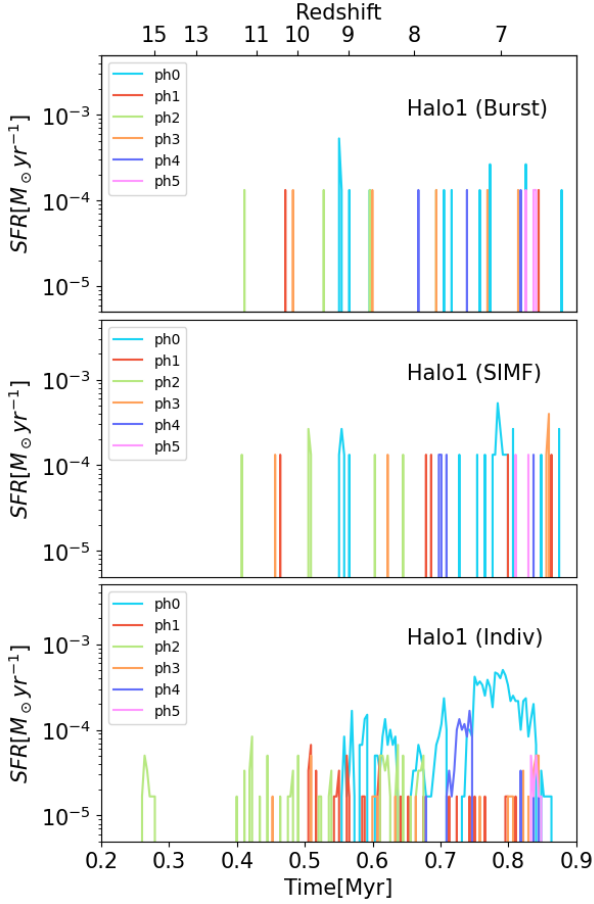


Figure 9. Star formation rates as a function of cosmic time are shown for the simulated UFD analogs, with different colors representing each progenitor halo. Note that the estimates are evaluated from all stars found in each halo, using a time bin of 3 Myr. This indicates that stars form in various environments rather than a single main progenitor. It also reveals that the IMF sampling method influences whether star formation will be discrete or continuous.

from 16% to 84%, indicating longer periods of continuous star formation. For example, in the case of ph0 (INDIV) for HALO1, stars are continuously formed for about 84% of the period. In contrast, the BURST and SIMF runs show that star formation occurs in less than 20% of the star formation period, indicating a highly sporadic and bursty pattern of star formation. Furthermore, the BURST runs are even more bursty compared to the SIMF runs, with the quenched period fractions exceeding 90%. Note that for low-mass haloes where initial star formation commences late and often stops before reionization, resulting in a single starburst, the quenching fraction cannot be determined for these haloes.

In terms of SFRs, the BURST and SIMF runs exhibit a highly bursty pattern, while the INDIV run shows a more continuous trend. However, regarding the frequency of SN events, the SIMF runs are expected to be as continuous as the INDIV runs since SNe are triggered with time lags in the SIMF runs. To quantify this burstiness, we use the B-parameter, as proposed by Applebaum et al. (2020). The B-parameter is defined as $B = (\sigma/\mu - 1)/(\sigma/\mu + 1)$, where σ is the standard deviation of the SN rate and μ is the mean SN rate. The SN rate is computed using a time bin of 3 Myr, yielding values between -1 and 1, with higher values closer to 1 indicating greater burstiness. In the BURST run, multiple SNe are triggered simultaneously each time

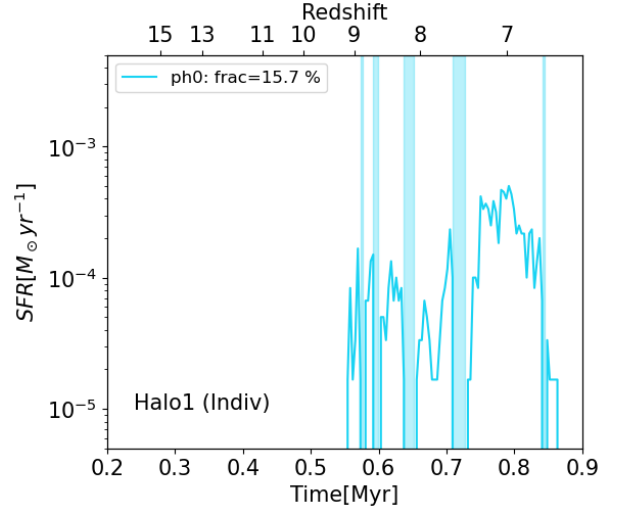


Figure 10. The star formation history of ph0 in HALO1 is presented. The quenched period fraction is determined by calculating the ratio of the total periods with no new star formation (shaded areas) to the overall star formation duration, which spans from the onset to the cessation of star formation in each progenitor halo. The estimated quenched period fraction of ph0 (INDIV) in HALO1 is 15.7%

a star particle with a mass of $500 M_{\odot}$ forms. On the other hand, for the SIMF run, although stars are sampled from a single SSP particle, the SN events occur at different times according to their individual lifetimes. Therefore, time delays are applied to each stellar particle to account for timing differences when computing the B-parameter.

As demonstrated in Fig. 12, the BURST runs tend to show high B-parameter values above 0.8, indicating high burstiness, whereas the values in the SIMF and INDIV runs are lower than those of the BURST run, implying a more continuous pattern. To sum up, in terms of SFRs, both the BURST and SIMF runs exhibit bursty patterns. However, when considering the SN rate, the SIMF runs are as continuous as the INDIV runs. Additionally, there is a trend that the B-parameter values decrease as progenitor masses increase, which is pronounced in the HALO1 case. This means that as the mass of the progenitor halo increases, burstiness decreases, and star formation occurs more continuously. This result concurs with the expectation that smaller haloes are more susceptible to feedback, easily quenching star formation.

3.2 Stellar abundance

3.2.1 Metallicity distribution function

Fig. 13 depicts the MDFs of stars formed in HALO1 (top panels), HALO2 (middle panels), and HALO3 (bottom panels), in each case. These results are compared with the composite MDFs of observed MW UFDs, represented by black lines (Fu et al. 2023), and those of UFDs in the Local Group (LG), shown as blue lines (Simon 2019). To ensure consistency, we adopt the method of Fu et al. (2023) to fit the MDF. This involves modeling the MDF of the simulated UFD analogs with a Gaussian distribution. We determine the best parameters for the mean and dispersion by maximizing the two-parameter Gaussian likelihood function (Walker et al. 2006), utilizing EMCEE to sample the posterior distribution. The resulting fits are illustrated as red lines in Fig. 13.

The MDFs of the simulated UFD analogs present the following characteristics: Firstly, the trend of enhanced stellar mass in INDIV runs, compared to BURST and SIMF under the same initial condi-

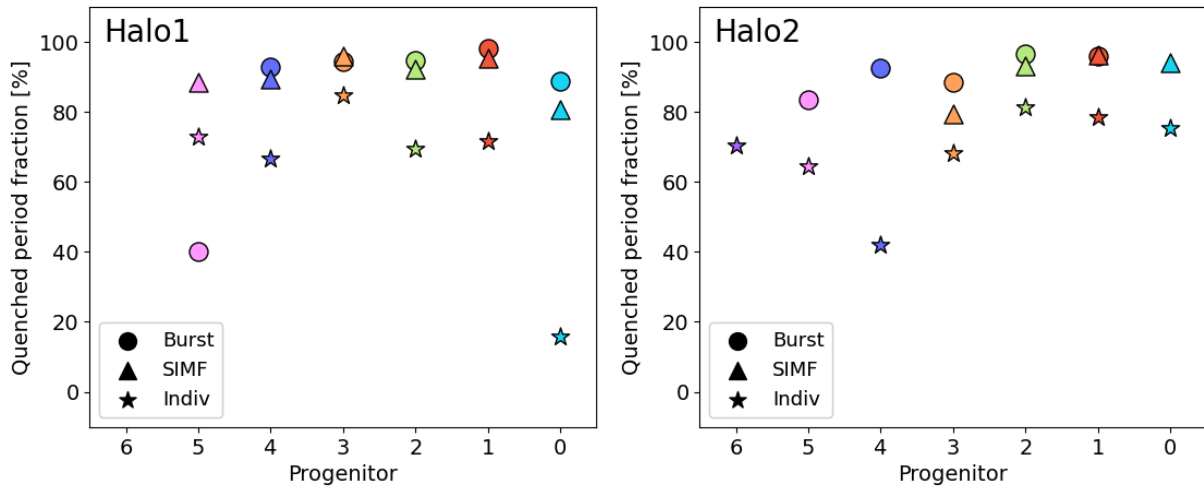


Figure 11. The quenched period fraction for progenitor haloes of HALO1 (left panel) and HALO2 (right panel). Due to the continuous nature of star formation in the INDIV runs, the quenched period fraction is lower compared to the BURST and SIMF runs. It also reveals that star formation in BURST is more likely to be sporadic and discrete than in SIMF. This is attributed to the powerful SN effect in the BURST runs, where multiple SNe are triggered simultaneously.

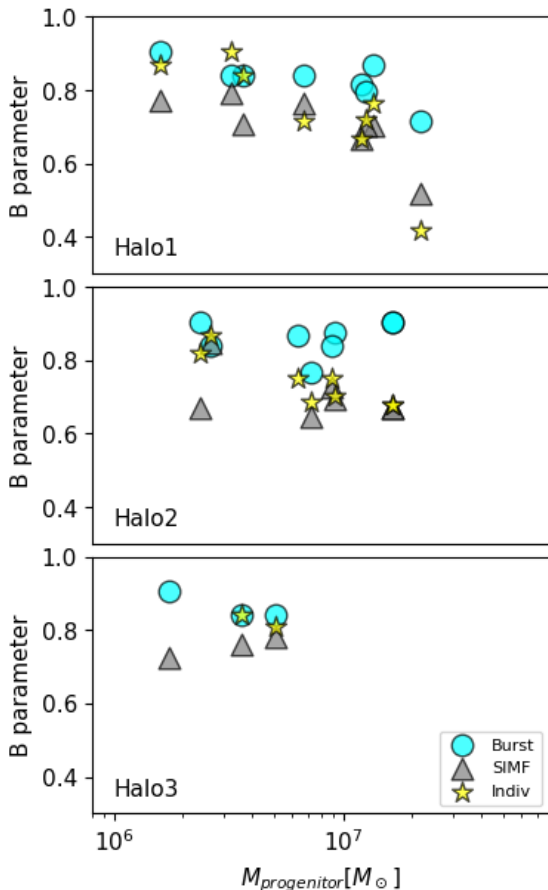


Figure 12. The B-parameter is used to measure the stochasticity of progenitor haloes in terms of SN rate, rather than SFRs. Specifically, in SIMF, although stars form simultaneously as a SSP, the SNe explode sequentially over time, resulting in a continuous SN rate. A B-parameter closer to 1 indicates a more continuous distribution. Unlike SFRs, the SIMF runs exhibit a more continuous trend, similar to or even more so than the INDIV runs.

tions, is similarly reflected in the stellar metallicity. For example, in HALO1, the average metallicity in INDIV ($\langle [\text{Fe}/\text{H}] \rangle = -2.20$) is 0.89 dex higher than in SIMF ($\langle [\text{Fe}/\text{H}] \rangle = -3.09$) and about 1 dex higher than in BURST ($\langle [\text{Fe}/\text{H}] \rangle = -3.21$). Furthermore, the MDF of INDIV for HALO2 matches closely with the observed data, whereas the MDFs for BURST and SIMF are skewed towards lower metallicities due to the absence of relatively high-metallicities ($[\text{Fe}/\text{H}] \gtrsim -2$). We find that in BURST and SIMF runs, there are no high-metallicity stars above $[\text{Fe}/\text{H}] = -2.1$. Meanwhile, in the INDIV runs, the maximum metallicity reaches $[\text{Fe}/\text{H}] = -1.21$ in HALO1 and $[\text{Fe}/\text{H}] = -1.41$ in HALO2. This difference arises from the smaller mass of SSP particles ($63 M_{\odot}$) in INDIV runs. This allows the star particles to rapidly reflect the gas metallicity contaminated by metals from previous SNe, leading to the formation of relatively higher metallicity stars.

Secondly, distinct from the observational data, which do not show stars with low-metallicity below $[\text{Fe}/\text{H}] = -4$, our results do feature such stars, which contribute to lowering the average metallicity. As discussed in Sections 3.1.3 and 3.1.4, these low-metallicity stars originate from external metal enrichment. We define stars formed through external metal enrichment as those initially outside the virial radius of the progenitor halo at formation, but later migrated inside. Another scenario that can produce low-metallicity stars involves star formation occurring at a density peak located on the outskirts of the progenitor halo, although still within the virial radius, thus classifying them as in-situ stars by definition. However, since this density peak is not self-enriching but instead polluted by metals from the inner regions, it leads to the formation of low-metallicity stars. The fraction of low-metallicity stars ($[\text{Fe}/\text{H}] \lesssim -4$) in INDIV is 3.5%, which is significantly lower compared to 31% in BURST and 28% in SIMF for HALO1. This occurs because, in INDIV runs, although low-metallicity SSPs with $m_{\text{PopII}} \approx 63 M_{\odot}$ may initially form due to external metal enrichment, subsequent in-situ stars continuously emerge from polluted gas. Meanwhile, in BURST and SIMF, a relatively large mass of stars ($m_{\text{PopII}} \approx 500 M_{\odot}$) are born with low-metallicity, which increases the fraction of such low-metallicity stars.

Thirdly, when in-situ star formation takes place, we find that the initial metallicity for Pop II stars, determined by Pop III stars, is approximately $[\text{Fe}/\text{H}] \approx -3$. This occurs because, to maintain consistency in our comparisons using different IMF sampling methods,

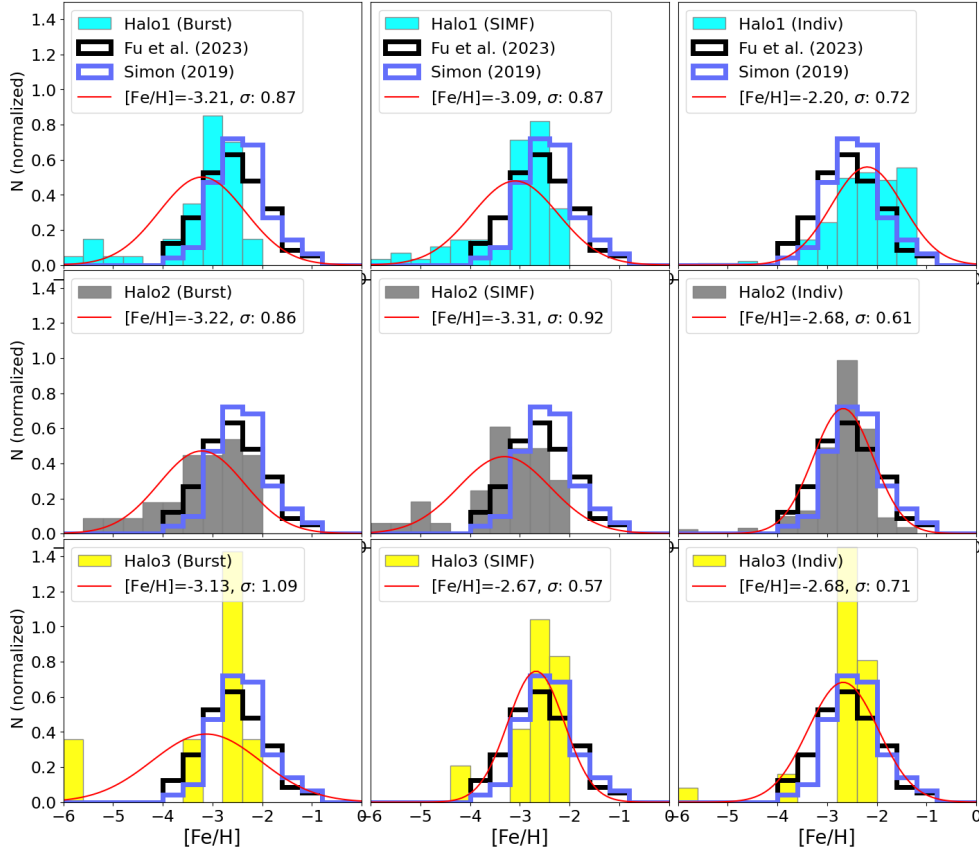


Figure 13. The metallicity distribution function for the simulated UFD analogs for HALO1 (top panels), HALO2 (middle panels), and HALO3 (bottom panels), compared with the composite MDFs of the observed MW UFDs, depicted by blue (Simon 2019) and black (Fu et al. 2023) histogram contours. Also, we provide a Gaussian fit (red solid line) characterized by its mean and dispersion values. It shows that due to the relatively large contribution of low-metallicity stars, $[\text{Fe}/\text{H}] \lesssim -4$, the dispersion of MDFs in the Burst and SIMF runs is larger than those in the INDIV runs by approximately 0.14 dex for HALO1 and 0.22–0.29 dex for HALO2. Note that the metallicities in HALO3 predominantly fall within the range of $[\text{Fe}/\text{H}] = -3.0$ to $[\text{Fe}/\text{H}] = -2.0$. This characteristic is attributed to one or two starbursts occurring at a later time, closer to the epoch of reionization.

we set the mass of Pop III stars to $m_{\text{PopIII}} = 20 M_{\odot}$. This setting typically establishes a metallicity floor of $[\text{Fe}/\text{H}] \approx -3$ in the gas where a Pop III SN explodes. However, this metallicity floor is rapidly altered by metals ejected from subsequent Pop II SNe.

Fig. 14 compares the estimates for the mean and dispersion of the MDFs of the simulated UFD analogs with those of 13 MW UFDs, as reported by Fu et al. (2023). The observed UFDs are color-coded based on their magnitudes, ranging from Draco II, with a low magnitude of $M_V = -0.8$, to Eridanus II, with a high magnitude of around $M_V = -7.1$. In the upper panel, all stars are included in fitting the MDFs, while the lower panel presents values derived after excluding stars with $[\text{Fe}/\text{H}] \lesssim -4$. This exclusion is due to the measured metallicity in Fu et al. (2023), using the MESA Stellar Isochrones and Tracks (MIST) models (Choi et al. 2016; Dotter 2016), being based on a metallicity grid ranging from $[\text{Fe}/\text{H}] = -4$ to $[\text{Fe}/\text{H}] = -1$. The results indicate that when no low-metallicity cut is applied, INDIV shows a dispersion value of $\sigma_{[\text{Fe}/\text{H}]} = 0.63 - 0.72$, which agrees with the upper limit of the observed dispersion values, and the average metallicity remains within the observed range. However, for BURST and SIMF runs, the average metallicity is about 0.5–1 dex lower than the observed ranges ($[\text{Fe}/\text{H}] \approx [-3.0, -2.0]$), and the dispersion is nearly twice as large.

By excluding low-metallicity stars, as shown in the lower panel of Fig. 14, a clear trend emerges: the estimated mean metallicities of

simulated UFD analogs, $\langle [\text{Fe}/\text{H}] \rangle$, decrease, matching closely with observational values. This exclusion also leads to a reduced dispersion in the MDF, which is associated with a shorter overall duration of star formation. This trend is particularly noticeable in HALO3, where the average dispersion across three different IMF sampling methods decreases to $\langle \sigma_{[\text{Fe}/\text{H}]} \rangle = 0.29$. In HALO3, star formation begins at a redshift of $z < 8$ and lasts for only about 20 Myr. Similarly, the average dispersions in the absence of low-metallicity stars are reduced to $\langle \sigma_{[\text{Fe}/\text{H}]} \rangle = 0.49$ in HALO1 and $\langle \sigma_{[\text{Fe}/\text{H}]} \rangle = 0.47$ in HALO2, showing good agreement with the observational findings.

3.2.2 Stellar mass - metallicity relation

We present the stellar mass- $[\text{Fe}/\text{H}]$ relationship in Fig. 15 based on our current simulations, compared with data from other high-resolution simulations, where the gas mass m_{gas} is between a few $10 M_{\odot}$ and $100 M_{\odot}$ (Wheeler et al. 2019; Agertz et al. 2020; Azartash-Namin et al. 2024), as well as with observational data (Kirby et al. 2013; Fu et al. 2023). The metallicity of observed MW dwarfs with stellar masses $M_* \lesssim 10^4 M_{\odot}$ falls within the range of $-2.5 < [\text{Fe}/\text{H}] < -1.7$ (Kirby et al. 2013; Fu et al. 2023). As noted by Fu et al. (2023), the observed UFD regime shows a plateau rather than a decreasing trend with diminishing luminosity. This indicates that the correlation between stellar masses and metallicity is rela-

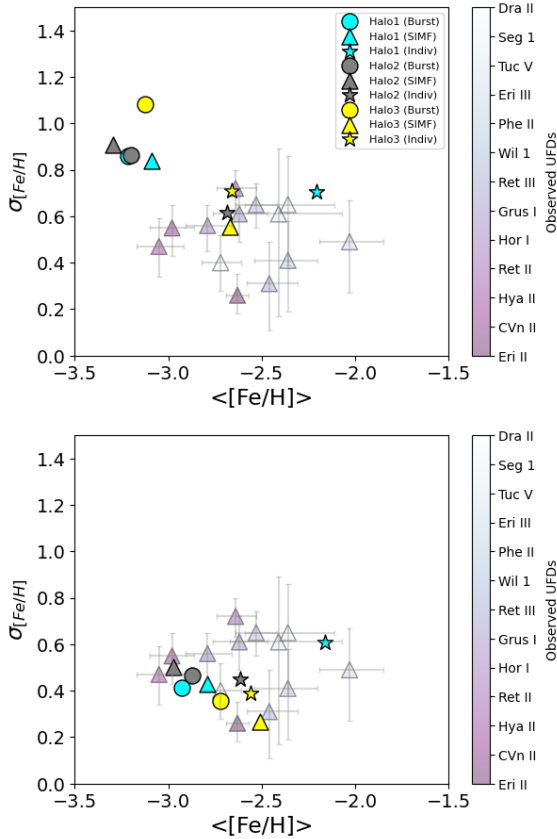


Figure 14. The best parameters for the mean and dispersion of MDFs of the simulated UFD analogs, based on all stars (top panel) and stars with metallicities above $[\text{Fe}/\text{H}] = -4$ (bottom panel). These parameters are then compared to the MDFs of the observed 13 UFDs reported by [Fu et al. \(2023\)](#). Excluding low-metallicity stars below $[\text{Fe}/\text{H}] = -4$ notably decreases the dispersions of the MDFs, bringing them into closer alignment with the observational findings.

tively weak compared to that found in more massive dwarf galaxies. Our results also support this observation, showing, for instance, that the lowest mass halo, HALO3, exhibits higher average metallicity values compared to the more massive halo, HALO2, by 0.65 dex (SIMF) and 0.07 dex (BURST). Specifically, in both scenarios—BURST and SIMF—where the burstiness in star formation is high, the correlation weakens as the stochasticity increases.

As demonstrated in Fig. 15, our results show that the metallicities from the INDIV runs show a good agreement with the observed values, whereas the BURST and SIMF runs exhibit metallicities that are 0.5 – 0.7 dex lower than the observed lower limit. This discrepancy occurs because, in the INDIV runs, the metallicity of gas enriched by earlier SNe is more rapidly incorporated into the newly formed stars. On the other hand, during BURST runs, where multiple SNe occur simultaneously within a SSP, the intense feedback significantly reduces the metallicity of stars formed afterward. In the SIMF approach, unlike INDIV, if the initial SN of an SSP does not halt star formation, subsequent SSPs form rapidly, leading to a starburst over a short period. This results in strong cumulative SN effects followed by a quenching phase. These powerful SN effects enhance metal diffusion, resulting in stars with lower metallicity compared to those formed in the INDIV run.

Previous theoretical studies have often struggled to reproduce the high-metallicity observed in the UFD regime. [Wheeler et al. \(2019\)](#)

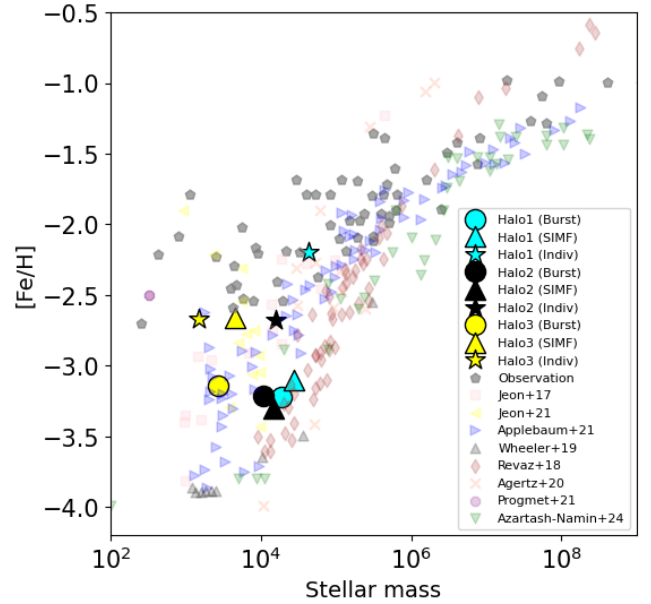


Figure 15. The stellar mass– $[\text{Fe}/\text{H}]$ relation of the UFD analogs obtained from the current simulations is compared to estimates derived from observations ([Kirby et al. 2013](#); [Fu et al. 2023](#)) and other theoretical studies ([Jeon et al. 2017](#); [Wheeler et al. 2019](#); [Agertz et al. 2020](#); [Applebaum et al. 2021](#); [Revaz et al. 2016](#); [Azartash-Namin et al. 2024](#)). It is evident that the estimated metallicities from the INDIV runs generally fall within the observed range, while the values from the BURST and SIMF runs are lower by ~ 1 dex compared to those of observed MW dwarf galaxies with stellar masses of $M_* \lesssim 10^5 M_\odot$. In particular, the SN feedback in the BURST runs might be too strong, causing metals to be expelled from the galaxies and reducing the metallicity of the gas clouds from which stars form.

suggested that lower metallicity compared to observations might be due to the absence of Pop III stars. However, as shown in our study, the contribution of Pop III stars is minimal because of a rapid transition from Pop III to Pop II star formation at early times. Likewise, [Sanati et al. \(2023\)](#) highlighted the challenge of increasing metallicity, even when considering metal contributions from Pop III SNe. As noted by [Jaacks et al. \(2019\)](#), pre-enrichment by Pop III stars appears insufficient to raise the metallicity floor beyond $[\text{Fe}/\text{H}] \gtrsim -4$, especially in low-density regions.

One possible factor leading to lower metallicity in theoretical models is the presence of excessively strong outflows that hinder the re-incorporation of ejected metals. [Agertz et al. \(2020\)](#) supports this idea, highlighting that strong feedback from SNe can expel enriched gas from a galaxy, thus decreasing the metallicity in star-forming clouds. The research by [Agertz et al. \(2020\)](#) also emphasizes the role of photoionization heating by stars, suggesting that heated gas is more likely to retain metals within the ISM. As a result, this enriched gas can give rise to stars with metallicities similar to observed values. Conversely, photoionization heating might lower metallicity by making SN feedback more effective at expelling metal-rich gas from a galaxy (e.g., [Jeon et al. 2014](#); [Smith et al. 2019](#)). The effects of stellar radiation on the metallicity of UFD analogs will be explored in future work.

Also, [Prgomet et al. \(2022\)](#) proposed a metallicity-dependent IMF as a solution to the discrepancy, where the IMF becomes more top-heavy with decreasing metallicity. This results in a higher fraction of massive stars in low-metallicity environments, enhancing SN feedback and photoionization heating, which suppress star formation

more effectively. Additionally, increased massive star production boosts metal output, reducing the stellar mass in UFD analogs while achieving metallicity levels comparable to those with a standard IMF. From an observational perspective, if we exclude low-metallicity stars ($[\text{Fe}/\text{H}] < -4$), as is done in observational studies, the average metallicity would increase by approximately 0.23 dex in HALO1, 0.24 dex in HALO2, and 0.25 dex in HALO3, potentially narrowing the gap between our results and the observations.

4 COMPARISON TO OTHER WORK

In the study by Applebaum et al. (2020), high-resolution simulations of MW-mass galaxies and isolated dwarf galaxies were performed, with an explicit incorporation of stochastic IMF sampling. The masses of DM particles, gas particles, and star particles were $1.0 \times 10^4 M_\odot$ ($1.8 \times 10^4 M_\odot$), $1.4 \times 10^3 M_\odot$ ($3.3 \times 10^3 M_\odot$), and $420 M_\odot$ ($990 M_\odot$), respectively, for isolated dwarf galaxies (the MW-mass galaxy). They compared two IMF sampling methods: one where SN feedback was discretized based on the sampled stars (stochastic IMF sampling), and another where SN feedback was implemented continuously using the IMF-averaged rate. The authors found that galaxies with halo masses $M_{\text{halo}} \lesssim 10^{8.5} M_\odot$ exhibit lower stellar masses when using stochastic IMF sampling compared to the IMF averaged rate. This is attributed to the bursty nature of SN feedback with stochastic IMF sampling, which effectively heats the surrounding gas, making low-mass galaxies particularly vulnerable due to their shallow potential wells.

Their findings are consistent with ours, as the burstiness of SNe, which influences the explosiveness of an event, is affected by the IMF sampling methods. The impact on the surrounding gas is more pronounced when SN energy is deposited in clusters rather than spread over time. Their study also explored the effects of stochastic IMF sampling on galaxy chemical enrichment, finding minimal impact on both the luminosity-metallicity relationship and the $[\text{O}/\text{Fe}]$ versus $[\text{Fe}/\text{H}]$ distribution. However, stars formed under stochastic IMF tend to have slightly higher $[\text{Fe}/\text{H}]$ values. These subtle differences are attributed to the efficient metal diffusion in the ISM, which diminishes the effects of IMF sampling. In contrast, our study, which uses higher resolution with gas particle masses around $63 M_\odot$, shows a noticeable difference. For instance, in the INDIV simulations, metals are more likely to accumulate in the surrounding gas due to relatively weaker SN effects, leading to the formation of high-metallicity stars compared to the BURST and SIMF simulations.

In a study conducted by Smith (2021), an idealized galaxy simulation was performed to examine the impact of IMF sampling on individual stellar feedback mechanisms, using a baryonic mass resolution of $20 M_\odot$. This study focused on an isolated dwarf galaxy with a virial mass of $M_{\text{vir}} = 10^{10} M_\odot$, and analyzed the effects of SN feedback, photoionization heating by stars, and photoelectric heating of dust grains. The aim was to compare the outcomes of using IMF-averaged feedback versus explicit stochastic sampling of the IMF. The findings revealed that when stellar feedback is restricted to SNe, the star formation rates are the same whether using stochastic IMF sampling or IMF-averaged feedback.

Rather, Smith (2021) suggested that photoionization heating by stars is the crucial factor distinguishing between the two IMF implementations, as it leads to more effective regulation of star formation with IMF-averaged rates compared to stochastic IMF sampling. In the IMF-averaged approach, each star generates H II regions with ionizing photons, whereas the stochastic IMF sampling run produces fewer H II regions associated with the stochastically selected stars.

Nevertheless, they cautioned that the effects of IMF sampling might change depending on the simulation's resolution or the feedback mechanisms applied. Also, Smith (2021) did not incorporate any physics related to metal yields. Considering their simulated galaxies are 100 times more massive than those in this study, it is anticipated that their galaxies are less affected by stochastic IMF sampling. Further research on the effects of stochastic IMF sampling with photoionization heating by stars in UFD regime is considered valuable and is planned for future work.

5 SUMMARY AND CONCLUSIONS

In our study, we examined the impact of various Initial Mass Function (IMF) sampling methods on the Star Formation Histories (SFHs) and metal enrichment histories of Ultra-Faint Dwarf (UFD) analogs using cosmological hydrodynamic zoom-in simulations. Achieving a high mass resolution ($m_{\text{gas}} \approx 63 M_\odot$) is essential for accurately resolving UFD analogs, the faintest galaxy systems in the Universe ($L < 10^5 L_\odot$) (e.g., Simon 2019). As mass resolution increases, it becomes necessary to revise existing sub-grid models, originally developed to represent baryonic physics in massive galaxies. Importantly, the method of IMF sampling plays a vital role in simulating UFD analogs, as it significantly influences the intensity of stellar feedback, especially supernova (SN) feedback, thus shaping the star formation and metal enrichment histories of the simulated galaxies.

Specifically, in this study, we conducted a series of hydrodynamic simulations on UFD analogs characterized by a virial mass of $M_{\text{vir}} \approx 2 - 8 \times 10^8 M_\odot$ and stellar masses of $M_* \lesssim 10^4 - 10^5 M_\odot$, comparing three different IMF sampling methods. The first method, called BURST, models stars to form continuously according to a given IMF but releases the entire SN energy all at once, significantly impacting the surrounding medium. The second method, named SIMF (Stochastic IMF), involves stochastically selecting the masses of stars, with SNe exploding one after another with a time lag during a single starburst, releasing SN energy discretely. This method better captures the discrete nature of SN events. The final method, INDIV, treats massive stars that will undergo SN explosions as individual star particles, while smaller stars ($m_* < 8 M_\odot$) are represented as a single stellar population (SSP). This method more realistically represents the stochastic nature of SNe, as each SN explodes individually, unlike the SIMF, which can result in multiple SNe originating from a SSP particle.

The main results are summarized as follows.

- Unlike massive galaxies, which primarily form stars in-situ within their main progenitor halo, we found that stars in UFD analogs originate from multiple progenitor haloes—typically 8 to 12 at $z = 6$ for $M_{\text{vir}} \approx 5 - 8 \times 10^8 M_\odot$ at $z = 0$. These progenitor haloes eventually merge to form a single UFD analog at a later stage. This pattern arises because star formation begins in several minihaloes of similar mass ($M_{\text{vir}} \approx 10^5 - 10^6 M_\odot$) at $z \gtrsim 14$ and ceases before reionization. Consequently, the identity of the primary halo can change, as no single halo consistently remains more massive than the others at high redshifts ($z \gtrsim 6$).

- The simulated UFD analogs in SIMF runs generally exhibit higher stellar masses, typically ranging from 40% to 70% more than those observed in the BURST simulations. This difference arises from the reduced impact of SNe in the stochastic IMF sampling approach. In both scenarios, stars form as $500 M_\odot$ SSPs. However, in the BURST simulations, the simultaneous explosion of multiple SNe immediately halts star formation. Conversely, in the SIMF simulations, if the most massive star in a SSP explodes as a SN but fails to disrupt the

surrounding medium, another $500 M_{\odot}$ SSP can form. As a result, the total stellar mass is higher in the SIMF simulations compared to the BURST simulations.

- Our findings indicate that simulated UFD analogs in the INDIV runs generate 8% to 58% more stellar mass compared to those in the SIMF runs. In the SIMF approach, if the first SN of a SSP does not inhibit star formation, subsequent SSPs form quickly, resulting in a starburst over a short duration. This leads to strong cumulative SN effects followed by a quenching period. By contrast, in the INDIV method, massive stars ($8 - 40 M_{\odot}$) form individually, with the formation of subsequent stars being more directly influenced by the impact of the preceding SN. Since the energy from a single SN is not overwhelmingly disruptive, star formation persists, particularly in areas with relatively massive progenitors. As a result, star formation is more continuous in the INDIV runs than in the SIMF runs.

- Regarding the star formation rate, star formation is most continuous in INDIV, followed by SIMF, and least continuous in BURST, leading to the highest quenching periods fraction in BURST. However, even though stars form in SSPs in SIMF, SNe explode stochastically over time, making the SN rate similarly continuous to that in INDIV.

- When comparing the metallicity distribution function (MDF) of observed UFDs with simulated UFD analogs, our results exhibit a low-metallicity tail ($[\text{Fe}/\text{H}] \lesssim -4$) that is rarely found in observations. Consequently, a Gaussian fit to the MDF of the simulated UFD analogs reveals a larger dispersion, about 0.28 dex greater than observed, particularly in the BURST and SIMF runs. We found that most of these low-metallicity stars ($[\text{Fe}/\text{H}] \lesssim -4$) formed through external metal-enrichment mechanisms.

- The average metallicity of the simulated UFD analogs, particularly in the INDIV runs, matches well with observed values. However, estimates in the BURST and SIMF runs tend to show lower $\langle [\text{Fe}/\text{H}] \rangle$ values by about 1 dex for stellar masses of $M_* \lesssim 10^5 M_{\odot}$ compared to observations. This difference can be attributed to the continuous nature of star formation in INDIV, where the gas metallicity shaped by previous SN events is rapidly reflected in the stellar metallicity, as stars are sampled individually. Moreover, the relatively weak energy from a single SN event in INDIV allows for continuous star formation, leading to stars with relatively high-metallicity ($[\text{Fe}/\text{H}] \gtrsim -2$).

UFDs are essential components in the hierarchical structure of larger galaxies and present invaluable opportunities to investigate the underlying mechanisms of galaxy formation and evolution. Despite being the faintest and most rudimentary systems, their physical properties are shaped by a complex interplay of baryonic processes, including star formation, stellar feedback, metal enrichment, and the dynamics of dark matter halo assembly. The properties of UFD analogs can vary considerably based on the sub-grid models employed to simulate these baryonic physics. Thus, it is imperative to advance theoretical research to develop and implement more sophisticated and realistic numerical models to enhance our understanding of UFDs. Alongside these theoretical developments, forthcoming observational data from next-generation telescopes, such as the Vera C. Rubin Observatory's Legacy Survey of Space and Time (LSST, [LSST Collaboration 2019](#)) and the Giant Magellan Telescope (GMT), is anticipated to significantly deepen our comprehension of the universe's smallest galaxy systems.

ACKNOWLEDGEMENTS

We extend our gratitude to Chanhee Shin for implementing the stochastic method in the code and for his assistance in writing the

manuscript. We also thank Volker Springel, Joop Schaye, and Claudio Dalla Vecchia for granting permission to use their versions of GADGET. M. J. acknowledges support from the National Research Foundation (NRF) grants funded by the Korean government (MSIT) under grant numbers 2021R1A2C109491713 and 2022M3K3A1093827.

DATA AVAILABILITY

The simulation data and results of this paper may be available upon request.

REFERENCES

- Abel T., Bryan G. L., Norman M. L., 2000, *ApJ*, **540**, 39
 Agertz O., et al., 2020, *MNRAS*, **491**, 1656
 Akins H. B., Christensen C. R., Brooks A. M., Munshi F., Applebaum E., Engelhardt A., Chamberland L., 2021, *ApJ*, **909**, 139
 Andersson E. P., Agertz O., Renaud F., Teyssier R., 2023, *MNRAS*, **521**, 2196
 Applebaum E., Brooks A. M., Quinn T. R., Christensen C. R., 2020, *MNRAS*, **492**, 8
 Applebaum E., Brooks A. M., Christensen C. R., Munshi F., Quinn T. R., Shen S., Tremmel M., 2021, *ApJ*, **906**, 96
 Azartash-Namin B., et al., 2024, *ApJ*, **970**, 40
 Barris B. J., Tonry J. L., 2006, *ApJ*, **637**, 427
 Behroozi P. S., Wechsler R. H., Conroy C., 2013, *ApJ*, **770**, 57
 Bovill M. S., Ricotti M., 2009, *ApJ*, **693**, 1859
 Brauer K., et al., 2024, *arXiv e-prints*, p. arXiv:2410.16366
 Bromm V., 2013, *Rep. Prog. Phys.*, **76**, 112901
 Bromm V., Kudritzki R. P., Loeb A., 2001, *ApJ*, **552**, 464
 Brook C. B., Di Cintio A., Knebe A., Gottlöber S., Hoffman Y., Yepes G., Garrison-Kimmel S., 2014, *ApJL*, **784**, L14
 Brown T. M., et al., 2014, *ApJ*, **796**, 91
 Bullock J. S., Kravtsov A. V., Weinberg D. H., 2000, *ApJ*, **539**, 517
 Carlin J. L., et al., 2019, *ApJ*, **886**, 109
 Choi J., Dotter A., Conroy C., Cantiello M., Paxton B., Johnson B. D., 2016, *ApJ*, **823**, 102
 Collins M. L. M., Read J. I., 2022, *Nature Astronomy*, **6**, 647
 Dalla Vecchia C., Schaye J., 2012, *MNRAS*, **426**, 140
 Deng Y., Li H., Liu B., Kannan R., Smith A., Bryan G. L., 2024, *arXiv e-prints*, p. arXiv:2405.08869
 Dotter A., 2016, *ApJS*, **222**, 8
 Durier F., Dalla Vecchia C., 2012, *MNRAS*, **419**, 465
 Emerick A., Bryan G. L., Mac Low M.-M., 2019, *MNRAS*, **482**, 1304
 Fan et al. 2006, *AJ*, **131**, 1203
 Ferland G. J., Korista K. T., Verner D. A., Ferguson J. W., Kingdon J. B., Verner E. M., 1998, *PASP*, **110**, 761
 Förster F., Wolf C., Podsiadlowski P., Han Z., 2006, *MNRAS*, **368**, 1893
 Fu S. W., et al., 2023, *ApJ*, **958**, 167
 Gallart C., et al., 2021, *ApJ*, **909**, 192
 Garrison-Kimmel S., Bullock J. S., Boylan-Kolchin M., Bardwell E., 2017, *MNRAS*, **464**, 3108
 Goater A., et al., 2024, *MNRAS*, **527**, 2403
 Greif T. H., Johnson J. L., Klessen R. S., Bromm V., 2009, *MNRAS*, **399**, 639
 Gunn J. E., Peterson B. A., 1965, *ApJ*, **142**, 1633
 Gutcke T. A., Pakmor R., Naab T., Springel V., 2021, *MNRAS*, **501**, 5597
 Haardt F., Madau P., 2012, *ApJ*, **746**, 125
 Haas M. R., Anders P., 2010, *A&A*, **512**, A79
 Hahn O., Abel T., 2011, *MNRAS*, **415**, 2101
 Heger A., Woosley S. E., 2002, *ApJ*, **567**, 532
 Heger A., Woosley S. E., 2010, *ApJ*, **724**, 341
 Heger A., Fryer C. L., Woosley S. E., Langer N., Hartmann D. H., 2003, *ApJ*, **591**, 288
 Hirano S., Hosokawa T., Yoshida N., Umeda H., Omukai K., Chiaki G., Yorke H. W., 2014, *ApJ*, **781**, 60

- Hirano S., Hosokawa T., Yoshida N., Omukai K., Yorke H. W., 2015, *MNRAS*, **448**, 568
- Hopkins P. F., Kereš D., Oñorbe J., Faucher-Giguère C.-A., Quataert E., Murray N., Bullock J. S., 2014, *MNRAS*, **445**, 581
- Hu C.-Y., Naab T., Glover S. C. O., Walch S., Clark P. C., 2017, *MNRAS*, **471**, 2151
- Jaacks J., Finkelstein S. L., Bromm V., 2019, *MNRAS*, **488**, 2202
- Jeon M., Pawlik A. H., Bromm V., Milosavljević M., 2014, *MNRAS*, **444**, 3288
- Jeon M., Besla G., Bromm V., 2017, *ApJ*, **848**, 85
- Jeon M., Bromm V., Besla G., Yoon J., Choi Y., 2021a, *MNRAS*, **502**, 1
- Jeon M., Besla G., Bromm V., 2021b, *MNRAS*, **506**, 1850
- Katz N., 1992, *ApJ*, **391**, 502
- Kirby E. N., Cohen J. G., Guhathakurta P., Cheng L., Bullock J. S., Gallazzi A., 2013, *ApJ*, **779**, 102
- Klessen R. S., Glover S. C. O., 2023, *ARA&A*, **61**, 65
- Klessen R. S., Lin D. N., 2003, *Physical Review E*, **67**, 046311
- Komatsu E., et al., 2011, *ApJS*, **192**, 18
- LSST Collaboration 2019, *ApJ*, **873**, 111
- Leroy A. K., Walter F., Brinks E., Bigiel F., de Blok W. J. G., Madore B., Thornley M. D., 2008, *AJ*, **136**, 2782
- Marigo P., 2001, *A&A*, **370**, 194
- McConnachie A. W., 2012, *AJ*, **144**, 4
- Munshi F., et al., 2013, *ApJ*, **766**, 56
- Munshi F., Brooks A. M., Applebaum E., Christensen C. R., Quinn T., Sligh S., 2021, *ApJ*, **923**, 35
- Navarro J. F., White S. D. M., 1993, *MNRAS*, **265**, 271
- Oñorbe J., Boylan-Kolchin M., Bullock J. S., Hopkins P. F., Kereš D., Faucher-Giguère C.-A., Quataert E., Murray N., 2015, *MNRAS*, **454**, 2092
- Omukai K., 2000, *ApJ*, **534**, 809
- Planck Collaboration 2016, *A&A*, **594**, A13
- Portinari L., Chiosi C., Bressan A., 1998, *A&A*, **334**, 505
- Prgomet M., Rey M. P., Andersson E. P., Segovia Otero A., Agertz O., Renaud F., Pontzen A., Read J. I., 2022, *MNRAS*, **513**, 2326
- Revaz Y., Arnaudon A., Nichols M., Bonvin V., Jablonka P., 2016, *A&A*, **588**, A21
- Rey M. P., Pontzen A., Agertz O., Orkney M. D. A., Read J. I., Saintonge A., Pedersen C., 2019, *ApJL*, **886**, L3
- Rey M. P., Pontzen A., Agertz O., Orkney M. D. A., Read J. I., Rosdahl J., 2020, *MNRAS*, **497**, 1508
- Safrank-Shrader C., Montgomery M. H., Milosavljević M., Bromm V., 2016, *MNRAS*, **455**, 3288
- Saitoh T. R., Makino J., 2009, *ApJ*, **697**, L99
- Sales L. V., Wetzel A., Fattahi A., 2022, *Nature Astronomy*, **6**, 897
- Salpeter E. E., 1955, *ApJ*, **121**, 161
- Sanati M., Jeanquartier F., Revaz Y., Jablonka P., 2023, *A&A*, **669**, A94
- Savino A., et al., 2023, *ApJ*, **956**, 86
- Sawala T., Scannapieco C., Maio U., White S., 2010, *MNRAS*, **402**, 1599
- Schaye J., et al., 2010, *MNRAS*, **402**, 1536
- Schmidt M., 1959, *ApJ*, **129**, 243
- Schneider R., Omukai K., 2010, *MNRAS*, **402**, 429
- Simon J. D., 2019, *ARA&A*, **57**, 375
- Simpson C. M., Bryan G. L., Johnston K. V., Smith B. D., Mac Low M.-M., Sharma S., Tumlinson J., 2013, *MNRAS*, **432**, 1989
- Simpson C. M., Grand R. J. J., Gómez F. A., Marinacci F., Pakmor R., Springel V., Campbell D. J. R., Frenk C. S., 2018, *MNRAS*, **478**, 548
- Smith M. C., 2021, *MNRAS*, **502**, 5417
- Smith M. C., Sijacki D., Shen S., 2018, *MNRAS*, **478**, 302
- Smith M. C., Sijacki D., Shen S., 2019, *MNRAS*, **485**, 3317
- Springel V., 2005, *MNRAS*, **364**, 1105
- Springel V., White S. D. M., Tormen G., Kauffmann G., 2001, *MNRAS*, **328**, 726
- Stinson G. S., Dalcanton J. J., Quinn T., Kaufmann T., Wadsley J., 2007, *ApJ*, **667**, 170
- Stinson G. S., Bailin J., Couchman H., Wadsley J., Shen S., Nickerson S., Brook C., Quinn T., 2010, *MNRAS*, **408**, 812
- Su K.-Y., et al., 2018, *MNRAS*, **480**, 1666
- Thielemann F.-K., et al., 2003, in Hillebrandt W., Leibundgut B., eds, *From Twilight to Highlight: The Physics of Supernovae*. p. 331, doi:10.1007/10828549_46
- Tolstoy E., Hill V., Tosi M., 2009, *ARA&A*, **47**, 371
- Walker M. G., Mateo M., Olszewski E. W., Bernstein R., Wang X., Woodroffe M., 2006, *AJ*, **131**, 2114
- Weisz D. R., Dolphin A. E., Skillman E. D., Holtzman J., Gilbert K. M., Dalcanton J. J., Williams B. F., 2014, *ApJ*, **789**, 148
- Wetzel A. R., Deason A. J., Garrison-Kimmel S., 2015, *ApJ*, **807**, 49
- Wheeler C., Oñorbe J., Bullock J. S., Boylan-Kolchin M., Elbert O. D., Garrison-Kimmel S., Hopkins P. F., Kereš D., 2015, *MNRAS*, **453**, 1305
- Wheeler C., et al., 2019, *MNRAS*, **490**, 4447
- Yoon S.-C., Dierks A., Langer N., 2012, *A&A*, **542**, A113
- Zhang E., et al., 2024, *ApJ*, **975**, 229

This paper has been typeset from a $\text{\TeX}/\text{\LaTeX}$ file prepared by the author.